NASA Technical Memorandum 110425

Further Developments of the Fringe-Imaging Skin Friction Technique

Gregory G. Zilliac, Ames Research Center, Moffett Field, California

December 1996

National Aeronautics and
Space Administration

Ames Research Center
Moffett Field, California 94035-1000

FURTHER DEVELOPMENTS OF THE FRINGE-IMAGING SKIN FRICTION TECHNIQUE

Gregory G. Zilliac

Ames Research Center

SUMMARY

Various aspects and extensions of the Fringe-Imaging Skin Friction technique (FISF) have been explored through the use of several benchtop experiments and modeling. The technique has been extended to handle three-dimensional flow fields with mild shear gradients. The optical and imaging system has been refined and a PC-based application has been written that has made it possible to obtain high resolution skin friction field measurements in a resonable period of time. The improved method was tested on a wingtip and compared with Navier-Stokes computations. Additionally, a general approach to interferogram-fringe spacing analysis has been developed that should have applications in other areas of interferometry. A detailed error analysis of the FISF technique is also included.

NOMENCLATURE

A	interferogram amplitude
a	wave amplitude or polynomial coefficient
B, P, E	low order polynomial coefficients
C	viscosity regression coefficients
d	diameter
h	oil film thickness
I	intensity
K	lens distortion coefficient
n	index of refraction, same as n_D (n at λ =2.320 $\times 10^{-5}$ in. or 589.2 nm)
p	pressure
q	dynamic pressure
Re	Reynolds number
r	radial distance measured from lens center
s	distance perpendicular to fringe bands ($s = 0$ at oil leading edge)
t	time
T	temperature
U_∞	freestream velocity
u, v, w	velocity components
w	distance between streamlines
x, y, z	surface coordinate system
α	oil coefficient of expansion or angle of attack
γ	specific gravity
δ	phase difference

Δs	fringe spacing (distance between peaks of destructive interference)
θ	circumferential direction
λ	illumination wavelength
μ	absolute viscosity
ν	kinematic viscosity or fringe visibility
ρ	density
ϕ	angle of c_f vector with $x - z$ plane
τ	skin friction

Subscripts

a	air
c	chord
cal	calibration
D	sodium spectral line
h	hydraulic
nom	nominal quantity
o	oil
$p - p$	peak to peak
T	temperature
w	wall
∞	freestream
$1, 2, \ldots$	fringe number (1 at first destructive interference, 2 at second . . ., etc.)

INTRODUCTION

Skin friction can account for half the drag (or more) of a flight vehicle. Attempts have been made to minimize this source of drag by increasing the laminar run on wings, using flush rivets and through the use of various boundary layer control devices. Only a small percentage of drag reduction attempts ultimately succeed. The failures often come at great expense. One of the reasons for this is that, until recently, no accurate methods existed to measure skin friction directly. To date, an accurate field measurement of a three-dimensional skin friction distribution, on a surface of aerodynamic interest, has not been achieved. In addition, turbulence modelers have a great need for skin friction data, particularly for off-cruise conditions where, typically, Reynolds-averaged Navier-Stokes (RANS) predictions of drag are 10% accurate at best.

Winter's extensive review paper (ref. 1) on skin friction measurement techniques quotes accuracies of 1.4%–10% for the most reliable and commonly used two-dimensional technique reviewed (the Preston tube). In a three-dimensional flow with a pressure gradient, even greater inaccuracies are to be expected using Preston tubes and most other skin friction measurement techniques.

The fringe-imaging skin friction technique (FISF) was developed by Monson and Mateer (ref. 2) and was inspired by the work of Tanner and Blows (ref. 3). Monson and Mateer measured the skin friction on a two-dimensional transonic airfoil and achieved a reasonable comparison with a Navier-Stokes solution.

2

The essence of the technique is that a simple expression relates skin friction to the thickness variation of an oil patch experiencing shear at a point on a surface. The oil-patch thickness variation is measured using interferometry. This technique is fundamentally similar to the laser-interferometer skin friction technique (refs. 4–7) except that the spatial variation of the oil-patch thickness is measured as opposed to the temporal variation. The accuracy and limitations of the two techniques are similar (±5%) but, inherently, the FISF technique is simpler and much less time consuming to use.

To date, the technique has been used successfully in several different two-dimensional flows to measure skin friction and also for transition dection, yet questions remain as to the effect of pressure gradients, high shear gradients, flow steadiness, and surface quality in addition to issues concerning implementation in a three-dimensional flow and determination of the fringe spacing from the interferogram images. To some degree, these questions have been dealt with by others (in particular, see refs. 2, 6–8). This work should be viewed as complementary to these studies.

For obvious reasons, extension of the FISF technique to three-dimensional flows is highly desirable. Monson and Mateer discontinued their development efforts after achieving a viable two-dimensional technique. In their approach, lines of oil were applied to the model surface normal to the nominal shear direction. In three dimensions, this approach will not work because the shear direction is usually not known a priori. In the current paper, oil drops (or dots), which are applied to the model surface and flow in the direction of shear, are explored for use in three-dimensional flows.

There are some drawbacks with the use of oil drops for three-dimensional skin friction measurements. The primary concern is that streamlines within the oil drops converge to an even greater degree than the streamlines of the outer air boundary layer in violation of the underlying FISF assumptions. As will be shown, streamline convergence increases the overall measurement uncertainty level in three-dimensional flows, but only slightly, and the advantages of this approach far outweigh the disadvantages for three-dimensional flows.

During the development of the current FISF methodology, an attempt was made to use inexpensive and readily available hardware and to develop user-friendly software that could be easily disseminated. In line with these goals, a 486-33 PC computer running Windows 3.1, Microsoft Visual C++ version 1.0, and Microsoft Fortran version 5.1 was used for software development and data acquisition. The cost of the complete measurement system (excluding computer) was under $1000, with the two most expensive items being a monochromatic CCD video camera and a frame grabber board.

CONSIDERATIONS

FISF Technique

A line (or drop) of silicone oil of known viscosity is placed on a prepared surface near the desired measurement location. The air flow is turned on and the oil spreads. After approximately two to ten

minutes, the oil forms a wedge with a nearly linear profile. The flow is turned off. At this point, an extended quasi-monochromatic light source, oriented nearly perpendicular to the surface, will create an interference pattern caused by the reflection of light from the top surface of the oil interfering with light reflected from the prepared test surface at the oil-surface interface. This pattern can be imaged using monochrome video camera. The distance Δs between the destructive interference bands of the interferogram is proportional to the thickness of the oil and, in turn, proportional to the skin friction (by lubrication theory) as follows:

$$c_f = \frac{\tau_w}{q_\infty} = \frac{2n_o\mu_o\Delta s}{q_\infty \lambda t} \tag{1}$$

for near normal illumination, and zero pressure and shear stress gradients.

The FISF approach and measurement procedure of the current study differ from reference 2 in several key areas. It was felt that, as suggested in reference 2, the technique should "stand alone" and not require a known reference skin friction value. Secondly, the light source, optics, and CCD camera have been built into a reasonably small box that approaches "point and shoot" ease of use. Thirdly, a fringe spacing identification algorithm has been developed, based on a firm theoretical foundation, that does not involve explicit image filtering or enhancement. Additionally, the current technique is fully three-dimensional and applicable to flows with moderate shear gradients. Finally, to maximize the data throughput, a PC-based Windows application has been written that integrates all of the required image acquisition and processing into one piece of software.

Numerical Modeling

The equation that governs the flow of oil on a surface with imposed pressure and shear gradients is (see fig. 1 for coordinate system definition):

$$\frac{\partial h}{\partial t} = \frac{1}{\mu_o}\left\{\frac{1}{3}\frac{\partial}{\partial x}\left(h^3\frac{\partial p}{\partial x}\right) - \frac{\mu_a}{2}\frac{\partial}{\partial x}\left[h^2\left(\frac{\partial U}{\partial y}\right)_{y=h}\right] + \frac{1}{3}\frac{\partial}{\partial z}\left(h^3\frac{\partial p}{\partial z}\right) - \frac{\mu_a}{2}\frac{\partial}{\partial z}\left[h^2\left(\frac{\partial W}{\partial y}\right)_{y=h}\right]\right\} \tag{2}$$

Squire (ref. 9) originally derived this expression by applying a conservation-of-mass control volume analysis of an oil film on a surface where the oil flow is described by the equations for slow viscous motion (which are obtained from the Navier-Stokes equations by neglecting the convective terms) with boundary conditions of an external air flow. The external air flow is described by the boundary layer equations. Coupling of the air and oil flowfields is achieved through the boundary condition at the air-oil interface ($y = h$) where the velocity and the shear stress of the air is specified to be the same as that of the oil. The assumptions made are that the oil flow is a two-dimensional, incompressible, slow viscous motion; the boundary layer thickness of the air is much greater than the oil thickness; and the pressure is constant normal to the surface (hence no surface tension effects are included). Note that in the above expression, upper case characters (U and W) refer to the air velocity and lower case refer to the velocity of the oil. If the air velocity is much greater than the oil velocity (in other words, μ_a/μ_o is small), then $(\partial U/\partial y)_{y=h}$ and $(\partial W/\partial y)_{y=h}$ are approximately τ_{xy}/μ_a and τ_{yz}/μ_a respectively. Furthermore, if the pressure gradient terms are small (as will be shown is the case for most real world
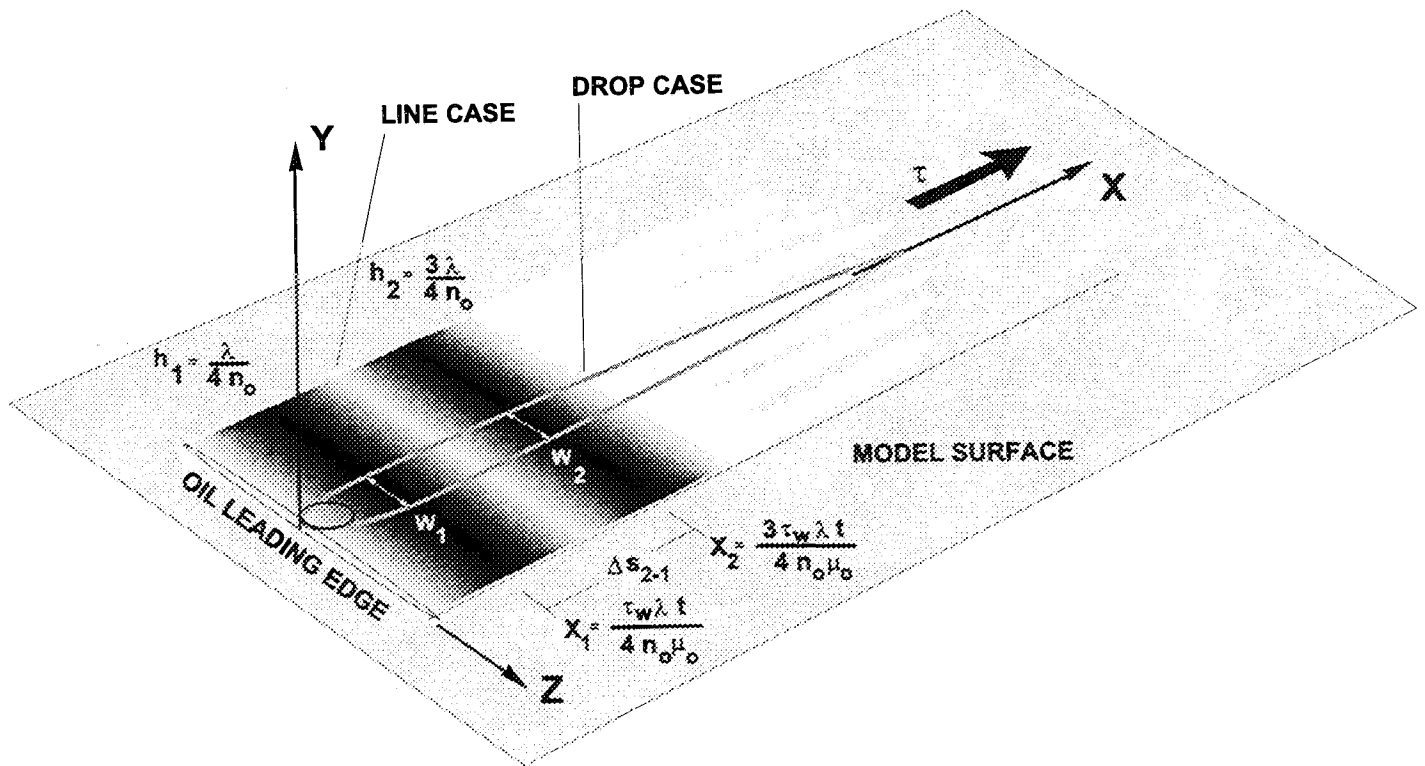
4

Figure 1. Oil film coordinate system definition.

aerodynamic problems) and the x coordinate direction is chosen so that it is aligned with the direction of the surface-shear stress, the defining equation becomes:

$$\frac{\partial h}{\partial t} = -\frac{1}{\mu_o}\frac{\partial}{\partial x}\left[\frac{h^2}{2}\tau_w\right] \tag{3}$$

A linearized solution can be found for this partial differential equation if it is assumed that τ_w is constant in x and t and that at $t = 0$, $h = \infty$. The solution is $\tau_w = \mu_o x / h t$ and this equation is the basis of the FISF technique (note that $x = 0$ at the leading edge of the oil). At this point, given all of the assumptions, one would have to question whether the FISF technique would be generally applicable to other than specialized situations. In particular, the assumptions of constant infinite initial oil thickness, of spatially constant τ_w, and that the oil flow streamlines are parallel are most bothersome.

To check the validity of the linearized solution of equation 3, the Lax-Wendroff algorithm was used to compute a finite difference solution to equation 3. Figure 2 shows the space-time development of an oil layer at a point on a surface under constant shear and pressure. As can be seen, after a brief onset period (less than 10 sec for this case) the analytical and finite difference solutions are in close agreement with one another. One point to note is that the oil never reaches a steady-state condition (h goes like $1/t$ at a given x location) although with time, the rate of oil-thickness change becomes small.

5

ANALYTICAL SOLUTION

- - - - - - LAX-WENDROFF SOLUTION

h (in.)

10^{-2} 10^{-3} 10^{-4} 10^{-5} 10^{-6} 10^{-7}

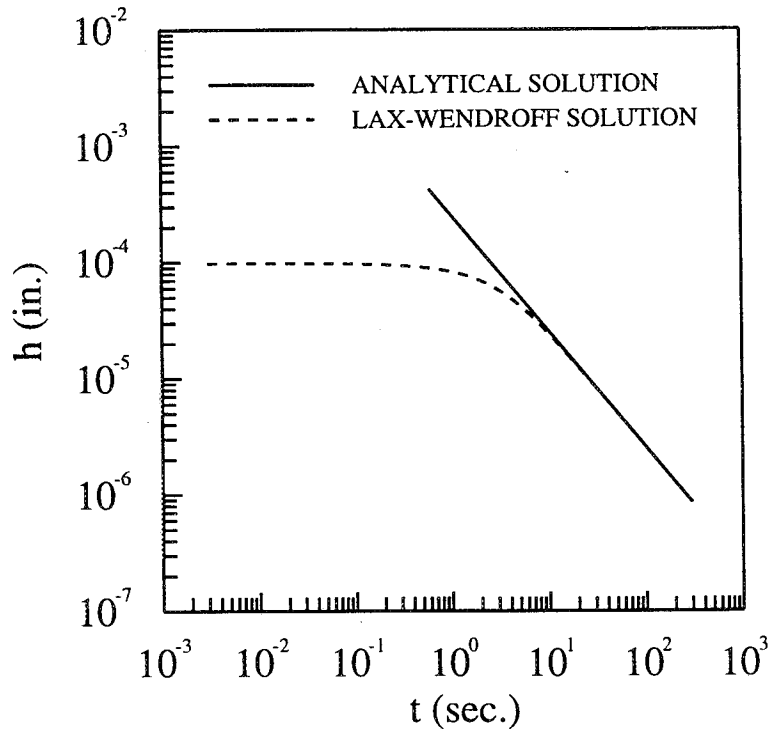10^{-3} 10^{-2} 10^{-1} 10^{0} 10^{1} 10^{2} 10^{3}

t (sec.)

Figure 2. Oil film thickness vs. time at $x = 0.146$ in. downstream of oil leading edge, $\tau_w = 0.05$ psf ($c_f = 0.00485$, $q_\infty = 10.39$ psf) and $\nu_o = 50$ cs.

Although the Lax-Wendroff based numerical model is deficient in that it does not properly model all of the initial transient effects (air boundary layer has been assumed to be steady and the time derivatives of the creeping oil flow have been neglected in the derivation of equation 3 (ref. 9)), it was found to be useful for several numerical experiments. Shown in figure 3 is the error inherent in determining the shear stress by $\mu_o x/ht$ as a function of time for various different initial configurations of the oil patch. The numerical solutions of three different initial oil-patch cross-sectional shapes (a half-ellipse, a sinusoidal leading edge, and a ramp) of three different initial maximum heights were computed and the resulting τ_w from $\mu_o x/ht$ compared with the constant τ_w imposed in the finite difference solution.

As expected, the results show that as time increases, the error of the linearized solution diminishes rapidly. What is surprising is that the cases with the elliptical initial shape approach the correct result at a higher rate than that of the ramp initial shape. This is fortunate because surface tension probably causes the leading edge of real life oil patches to to take on an initial shape that is approximately elliptical.

Another unexpected result is that the error is less for the cases that had a greater initial oil thickness. This is evidence that a thick initial oil distribution probably more closely approximates the infinite oil layer thickness initial condition assumption of the linearized solution. So even though, in practice, it is difficult to apply oil to a surface in a repeatable fashion, if the quantity of oil is sufficient and the oil is allowed to flow for a long enough time, the solution predicted by $\tau_w = \mu_o x/ht$ is probably accurate to within a small fraction of a percent.
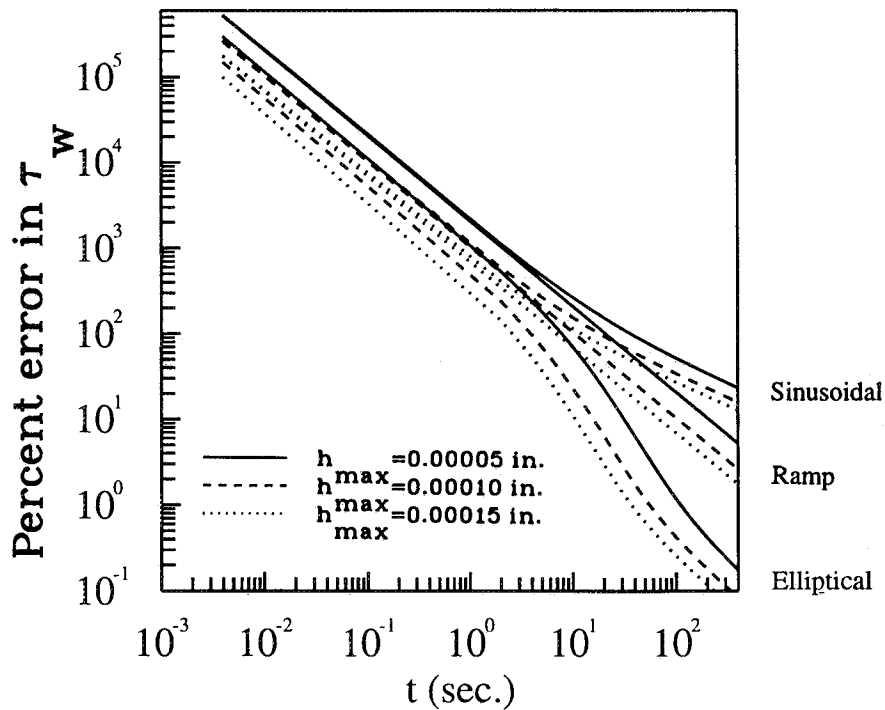
6

Figure 3. Percent error owing to differences in oil film initial conditions, $\tau_w = 0.05$ psf ($c_f = 0.00485$, $q_\infty = 10.39$ psf) and $\nu_o = 50$ cs.

Two additional comments should be made concerning the linear expression ($\tau_w = \mu_o x / ht$). Since it is derived using the boundary layer approximation for the oil flow, it is highly unlikely that it is valid on highly curved surfaces. Secondly, in a strict sense, it is only valid for laminar air flows because the air-oil interface boundary conditions ($U = u, W = w, \mu_a \frac{\partial U}{\partial y} = \mu_o \frac{\partial u}{\partial y}, \mu_a \frac{\partial W}{\partial y} = \mu_o \frac{\partial w}{\partial y}$ at $y = h$) are laminar conditions but, using Squire's analysis, one can show that the analytical solution to equation 3 is the same for a turbulent air flow with the predicted shear stress τ_w being a time-average quantity. This result is supported by reference 8 where numerical experiments showed that the instantaneous rate of change of the thickness of an oil film responds very rapidly, hence τ_w determined from equation 1 should be the correct time-averaged result in a turbulent (also an unsteady) flowfield. These conclusions are surprising considering that the time derivatives in the creeping-motion oil flow model were neglected, but in reference 8 it is argued that these terms become significant only when the frequency of interest is $O(\nu_o/h^2)$ (e.g., 3 kHz is a conservative estimate if $\nu_o = 5.4 \times 10^{-4}$ ft^2/sec or 50 cs and $h = 0.002$ in. at the start of a run for a low speed case).

Optical and Imaging Systems

A wide variety of optical configurations can be used to create the interferograms as part of an FISF system. The simplest consists of a scale and a fluorescent lamp. If a fluorescent lamp is held in such a manner that its reflection is visible in the surface of the oil, a fringe pattern will also be visible in the surface of the oil provided the oil is sufficiently thin. A fringe, in the following discussion, is defined as the line formed by the destructive interference of the light reflection, and the fringe spacing is the distance between these dark bands.

7

Since a fluorescent lamp is not a monochromatic light source, the fringes will be made up of several different colored bands but a rough measurement using a scale can still be made between bands of the same color. If an interference filter (a narrow bandpass filter) is placed between the light source and the oil, only the spectral components near the center wavelength of the filter will be transmitted resulting in a quasi-monochromatic fringe pattern.

A relatively inexpensive yet accurate and highly portable optical system can be made by substituting an HeNe laser diode and a spherical lens for the light bulb in a lighted reticle (all necessary components available through Edmund Scientific, Barrington, NJ). A note of caution: Some lasers (particularly laser diodes) can have significant wavelength dependencies on ambient temperature.

In an attempt to improve upon the optical system used in reference 2, several different types of light sources in combination with lens, filters, diffuser sheets, and test surfaces were tried. The various optical system configurations were investigated by using the FISF technique to evaluate the interferometric image created by a channel-flow shear field.

The 0.25 × 2.0 in. channel flow facility is a shop-air powered rectangular channel that is 48 in. long with inlet flow conditioning and interchangeable test surfaces. Under normal operating conditions ($q_\infty = 2.1$ in. water, $d_h = 0.44$ in., and $Re_{d_h} = 2.3 \times 10^4$), a fully developed channel flow with a uniform shear field and a nominal constant c_f of 0.00485 is created. The reference test surface was a piece of 0.25 in. thick SF11 Schott glass polished to better than 60/40 scratch and dig, and coated on the back side with 1/4 wave MgFl to minimize reflections of the light from the back-side glass-air interface back through the oil. This particular glass has an index of refraction of 1.78 giving a theoretical fringe visibility of $\nu = 0.94$ (for $n = 1.4$ silicone oil).

Initially, it was thought that a laser would be the best light source choice because lasers are highly monochromatic and have the desirable characteristic of a coherence length that is many times the oil layer thickness (measured in inches to feet for gas lasers and typically less than 0.040 in. for HeNe diode lasers). This proved not to be the case because of difficulties with speckle. The peak-to-peak intensity variation of the first fringe on SF11 glass was 121 intensity levels (using an 8-bit camera which has 256 levels in total) with the speckle causing a 20 intensity-level variation superimposed on that of the interferogram. Unfortunately, short of applying exotic techniques (e.g., a rotating ground glass piece in the light path), there is no easy way to avoid the speckle that will be present in systems with highly coherent light sources and diffusing optical components.

Another approach attempted was to use a thermal source (Philips Halogen spot lamp model PAR16/H/NSP, Philips Lighting Company, Somerset, NJ) combined with a bandpass interference filter. The OCLI (Santa Rosa, CA) Green Dichroic filter had an FWHM (full width measured at half transmittance) of 2.76×10^{-6} in. (70 nm) centered on a wavelength of 2.13×10^{-5} in. (540 nm). The peak-to-peak intensity variation of this combination was quite poor, being less than 30 intensity levels. In addition, the amount of heat generated by this source was potentially damaging to the interference filter and the pellicle beam splitter.

The light source finally settled on was a green 9-watt compact fluorescent lamp (Osram Corp. model F9TT/Green, Montgomery, NY). This lamp has a sharp spectral peak at 2.13×10^{-5} in. (542 nm) and several much smaller peaks approximately 1.58 to 1.97×10^{-6} in. (40–50 nm) to either side of the main

8

peak and farther away. These additional peaks were effectively blocked by the OCLI green interference filter. The Osram lamp has a coherence length of 5.9×10^{-5} in. (15 μm), nearly 30 times the path difference at the first fringe. The first-fringe peak-to-peak intensity variation was 124 intensity levels on SF11 glass and additionally, the lamp runs fairly cool.

As shown in figure 4, the lamp was mounted in an aluminum chassis along with a black and white 1/3 in. CCD camera with an 0.3149 in. (8 mm) focal length lens, a bandpass interference filter, a 50%-50% pellicle beam splitter and an opal diffusing sheet. The CCD camera was hooked up to an eight-bit frame grabber board (model CX-100, ImageNation Corp., Beaverton, OR) and also a monitor. The beam splitter allows for near normal illumination and imaging of the fringes. A seemingly insignificant (but crucial) component of the system is the opal diffusing element. This sheet combined with the diffuse light emanating from the compact fluorescent creates an "extended" light source. A pellicle beam splitter was chosen over plate glass or cube type splitters to minimize problems associated with ghosting and astigmatism. As an aside, an extended light source (as opposed to a distant point light source which generates parallel light rays) is necessary because interference fringes can be seen or imaged only if there is a small variation in the incidence angle of the light hitting the oil surface (in addition to the phase shift caused by the oil).

One small problem in using a fluorescent light source is that, depending on the type of ballast used, flicker (an intensity oscillation) can be quite substantial. Initially, an electromagnetic ballast was used and it was determined by photo diode measurements that the intensity variation was approximately 50% of the mean at a frequency of 120 hertz. As one can imagine, fluctuations of this magnitude, coupled with the interlaced scanning methods used in many CCD cameras, can lead to significant errors in the imaged fringe spatial intensity variation. This difficulty was overcome through the use of an electronic ballast that was taken from the base of an off-the-shelf Edison-bulb socket to compact fluorescent converter (Light's of America model 5509, Walnut, CA). Use of this electronic ballast reduced the flicker by a factor of five.

An even greater flicker reduction could be obtained by use of a more sophisticated high-frequency (20 kHz) electronic ballast typically used in large fluorescent lamps but such a ballast was not readily available for a 9-watt lamp. One could build such a ballast by modifying the circuit design shown in reference 10 but, in the current study, time constraints did not permit this undertaking. In any event, modeling of the impact of the reduced flicker level on fringe identification showed that it will have virtually no impact on the overall accuracy of the technique.

Fringe Identification

The chief difficulty in identifying the imaged interferometric fringe spacing is that, on a line perpendicular to the fringes, typically, only 15 to 60 data points per fringe (pixels between successive lines of destructive interference or "dark bands") are imaged using the previously described optical system (which includes an eight bit, 512×512 CCD camera). At most, only the first two fringe spaces should be used, because if additional fringes are used internal reflections in combination with noise, shear, and pressure gradient effects will decrease the overall accuracy of the identification.

CHASSIS

FRAME GRABBER TRIGGER

8-BIT CCD CAMERA

BAFFLE

CAMERA LENS

COMPACT FLUORESCENT
LIGHT SOURCE

50/50 PELLICLE
BEAMSPLITTER

INTERFERENCE FILTER AND
OPAL DIFFUSING ELEMENT

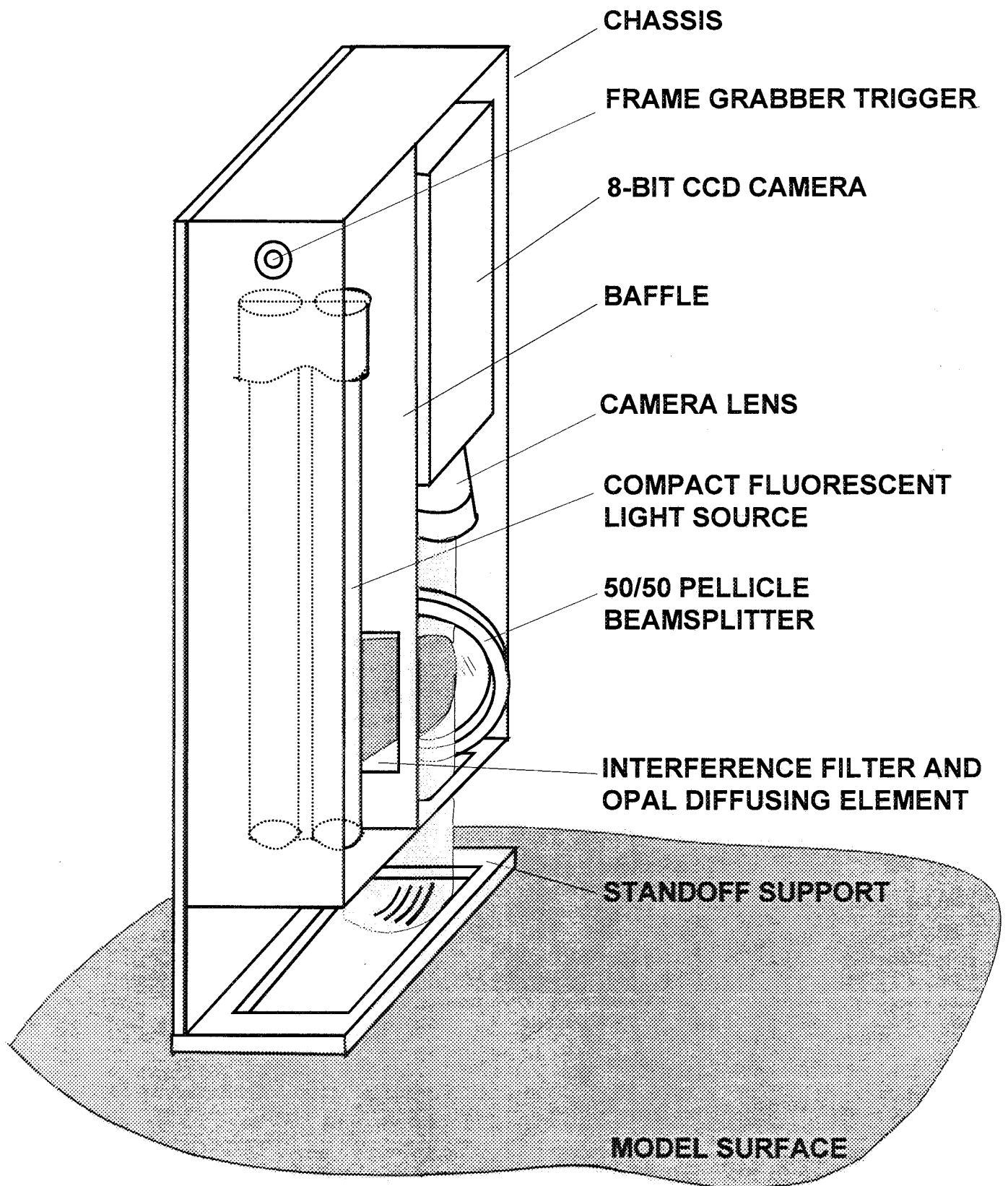STANDOFF SUPPORT

MODEL SURFACE

Figure 4. The FISF instrument box (cover removed).

Several approaches to identification of the fringe spacing were attempted in the current study, namely, techniques that involved fast Fourier transforms, linear least-squares curve fitting, correlation of trigonometric functions, maximum entropy determination (ref. 11) and nonlinear least-squares regression. With the exception of the nonlinear least-squares regression approach, the other approaches were found to be inadequate.

In the cases of the fast Fourier transform and maximum entropy methods, the record length (number of pixels imaged) was too few to achieve sufficient resolution of the spectral peaks. Additionally, with short records, FFTs shift the spectral maximums. In fact, it has been shown that when the record length of a truncated sinusoid is less than 0.58 times the period, the spectral peak is found at zero (ref. 11).

The piecewise polynomials approach—where polynomials were fitted to the fringe-pattern crests and troughs and fringe spacings determined—failed because the local effect of "noise" (undesirable effects arising from background irregularities, the CCD camera, and lighting nonuniformities) over-whelmed the local data fits.

A slightly more successful but not wholly satisfactory approach involved maximizing the product of a cosine function (with wavelength and phase as variable parameters) and the imaged signal. The basis of this approach is that, theoretically, the spatial intensity variation of an interferogram is describable by trigometric functions. The downfall of this "correlation" approach is that a simple cosine variation does not include the effect of intensity variations arising from curved surfaces and nonuniform lighting. Consequently, in these cases correlation maximums were found for fringe spacings that were obviously erroneous.

The marginal success of the "correlation" approach led to the development of a general fringe-intensity-variation model. The intensity distribution of simple interferogram (Young's fringes) created by the interference of two beams of monochromatic light of equal intensity and initially in phase with each other is $I \approx A^2 = 2a^2(1 + cos\delta)$. Based on this expression, one can imagine that the intensity variation of an interferogram of greater complexity, such as that generated on a surface with mild curvature, illuminated with slightly nonuniform light, could be represented by a nonlinear function constructed using quadratics as follows:

$$I = B_1 + B_2s + B_3s^2 + \left[E_1 + E_2s + E_3s^2\right] cos\left[P_1 + P_2s + P_3s^2\right] \tag{4}$$

This model, which is similar to that used in reference 12, has nine parameters, each of which has physical significance. The trick is to determine the unknown B, E, and P coefficients so that equation 4 best represents the digitized intensity variation. For this task, the quasi-Newton method was used as described in reference 13. In short, the numerical technique uses an initial "best guess" for $B, E,$ and P of the intensity variation and then iterates until the difference between the discrete input data points and the I polynomial is within some convergence tolerance. Examples of typical regression results, for a high quality fringe intensity variation (obtained on an SF11 glass surface) and also a marginal variation (polished 304 stainless steel surface) are shown in figure 5.
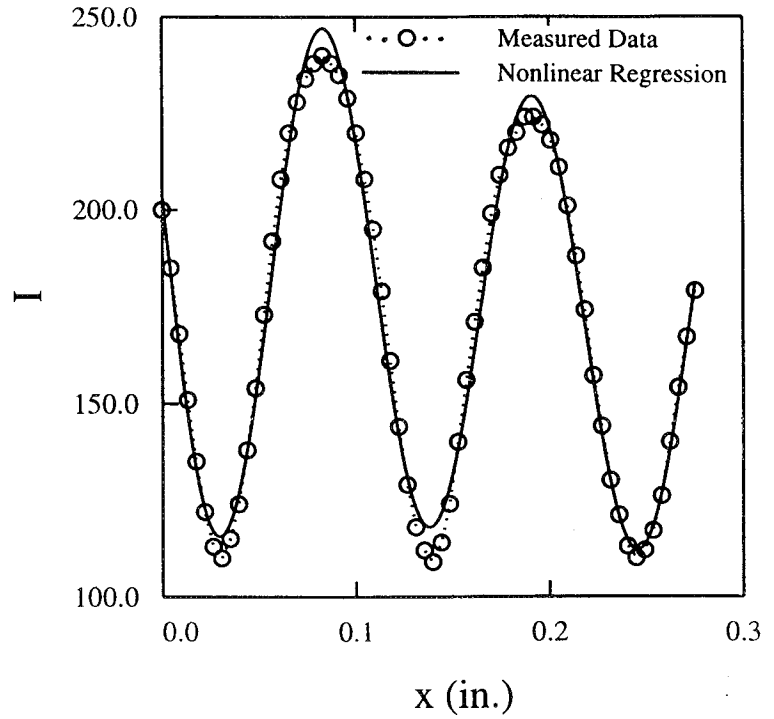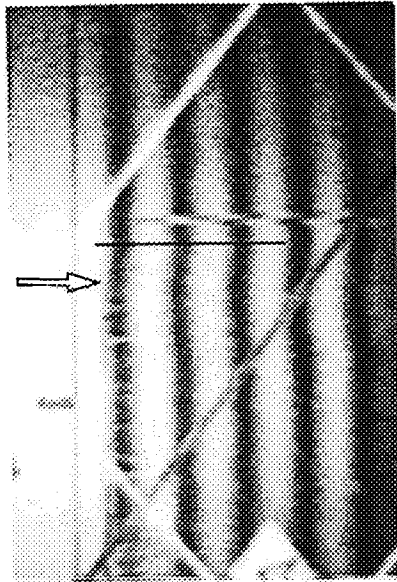
Figure 5(a). Nonlinear regression applied to a typical fringe intensity variation on an SF11 glass surface (8-bit CCD camera).
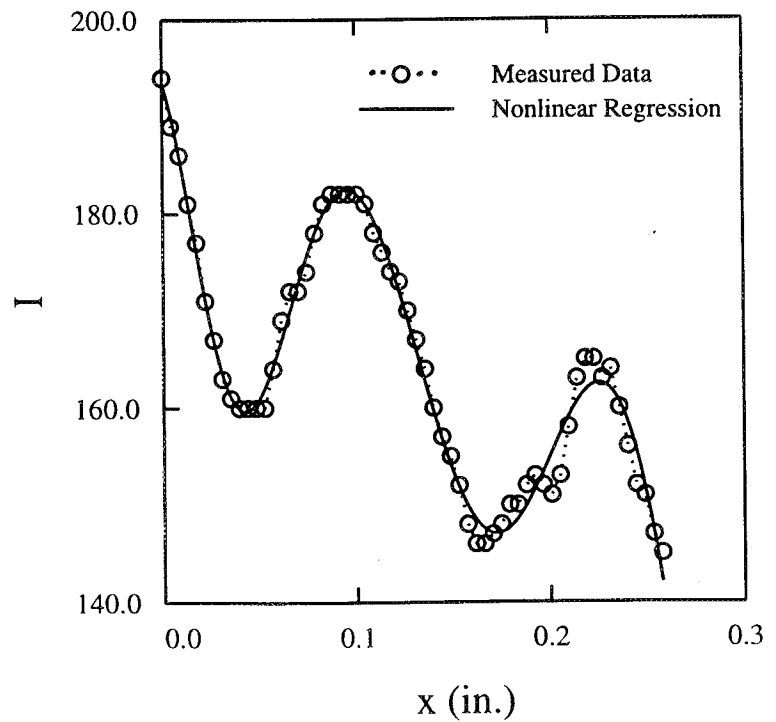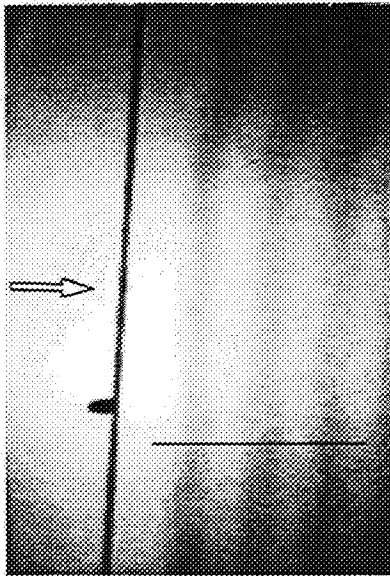

Figure 5(b). Nonlinear regression applied to a typical fringe intensity variation on a polished 304 stainless steel surface (8-bit CCD camera).

12

There are a couple of difficulties. If the initial guess is not a reasonable one, the convergence process can get trapped in a local minimum. Also, extremely noisy input data can cause convergence problems. In most cases, the method is reliable and, as will be shown, fairly accurate.

In the current approach, a weighting function has been implemented in the quasi-Newton method so that the error between the output polynomial and the input data is minimized when dI/ds is high. High dI/ds occurs midway between the destructive and constructive interference bands. The justification for use of weighting is that the effect of noise in the signal of the CCD based imaging system has the least impact where the intensity variations are large.

Fringe Visibility

As stated in the Introduction, obtaining good fringe visibility when using the FISF technique under less than ideal conditions can be difficult. Fringe visibility can be defined as $\nu = (I_{max} - I_{min})/(I_{max} + I_{min})$ (where I_{max} and I_{min} are the fringe intensity maximums and minimums) and is a measure of the contrast between the bands of constructive and destructive interference.

Theoretically, for the FISF technique, the maximum fringe visibility ($\nu = 1.0$) is achieved on a surface of $n = 2.0$ (for $n = 1.4$ silicone oil) observed at infinity with an extended monochromatic source. The constraints in most real life measurement situations usually result in fringe visibilities of 0.5 or less. For instance, wind tunnel models are usually made of less than optimal interferometry surface materials such as steel or aluminum, and these models must be polished to near mirror-quality finish or be coated by a material with more desirable optical properties.

The ideal FISF surface has the properties of being very smooth (60/40 scratch and dig, or better), has optical properties that remain constant (does not haze or corrode over time), can be cleaned and reused, and is scratch resistant. As part of the current study, many different kinds of coatings were tried, and although nothing approaching the quality of a dense flint glass was identified, a few acceptable coatings were found.

Shown in table 1 are the results of an investigation into several candidate surface materials. The data were obtained using the FISF system (shown in fig. 4) and channel test facility previously described. A line of $\nu_o = 5.4 \times 10^{-4}$ ft²/sec (50 cs) oil was placed on a candidate surface in the channel, and fringes were generated under constant shear conditions. The resulting c_f measurements were within 5% of each other (better than the FISF uncertainty quoted in ref. 2) for all of the surfaces studied. This is additional evidence that surface tension effects have a minimal impact on FISF measurements. Each datapoint in table 1 is an average over ten trials of first fringe data. In evaluating a candidate surface material, the most useful data is the peak-to-peak first fringe intensity measurement (I_{p-p}) since the overall accuracy of an FISF measurement is directly related to this quantity. Also presented are values for $I_{(p-p)_{rms}}$, which can be considered to be a measure of the quality of the fringes, and I_{avg}, which is average intensity of the imaged fringe.

A couple of disclaimers are in order. It was found that the index of refraction of the surface material can vary by a significant amount depending on the surface preparation, the material batch, oxidation, and other factors. In addition, the automatic electronic shuttering capability of the CCD camera determines

the exposure time based on a large portion of the field of view and no attempt was made to adjust the exposure to maintain a constant average fringe intensity level from case to case. So the numbers in table 1 should be taken as representative and not necessarily as the best that can be achieved.

Note that the transparent surface finishes were applied over a black coating in order to maximize the absorbtion of the transmitted light (backside of materials in sheet form were painted black).

The data in table 1 show that the best FISF surface material of those studied is the high flint content SF11 glass. This is not surprising because the index is the highest. Unfortunately, few wind tunnel models can be made of glass. From the standpoint of fringe intensity, the best spray-on surface coating is the ElectraMates Epoxy coating, although the Zynolyte epoxy paint was found to produce fringes of very high quality and results that were very repeatable as evidenced by the low $I_{(p-p)_{rms}}$. Of the plastic sheet materials, black Ultem 1000 and Mylar were approximately equal. This is not surprising because they have approximately the same index of refraction ($n = 1.67$). Finally, polished 304 stainless steel is preferable to polished 1024 aluminum but is marginal as an FISF surface.

It may be possible to develop a spray-on monomer (or plastic) coating with an index of refraction approaching $n = 1.7$. The highest index of refraction plastic identified is a polyetherimide (PEI) thermoplastic (trade name of Ultem 1000, General Electric Corp. Pittsfield, MA 01201) with a refractive index of 1.67. This plastic is currently available in thin sheets and possibly could be made into a spray-on coating using the solvent methylene chloride (unfortunately, a fairly toxic solvent). One advantage

Table 1. Characteristics of various surface materials (8-bit imaging system, $I_{max} = 256$)

Surface material	I_{avg}	I_{p-p}	$I_{(p-p)_{rms}}$	Remarks
SF11 Glass Shott Glass Co., Mainz, Germany	186.0	123.8	6.8	best fringes
Epoxy Rust-Mate Spray Zynolyte Products Co., Carson, CA	168.1	31.3	2.8	
ElectraMates Insulating Epoxy Coating Aervoe-Pacific Co., Gardnerville, NV	150.8	56.6	5.0	
Clear Acrylic Spray no. 117 Aervoe-Pacific Co., Gardnerville, NV	153.4	36.5	4.0	relatively rough, short fringe life
5-mil Vinyl Sheet Tap Plastics, Dublin, CA	155.5	49.7	4.6	difficult to apply
Black Ultem 1000 Sheet Westlake Plastic Co., Lenni, PA	153.1	87.6	6.7	
P.S. Mylar Sheet Tap Plastics, Dublin, CA	158.6	90.7	7.9	backside painted black, very smooth surface
2024 Aluminum	171.4	9.4	2.9	mirror finish
304 Stainless Steel	185.0	26.6	2.5	mirror finish

14

of this plastic is that it can be flame polished (approximately 650°F melting point) to remove small surface imperfections. Application of the FISF technique on an Ultem 1000 surface should result in a theoretical fringe visibility of 0.82.

Pressure Gradient Effects

The effect of pressure gradients on FISF measurements is very small and can be ignored in virtually all cases. By examining the order of magnitude of the terms in equation 2, it can be seen that the pressure gradient terms are at least two orders of magnitude smaller than the shear stress terms for most flows of aerodynamic interest.

Direct evidence of the insignificance of pressure gradient effects was obtained through numerical experiments using the Lax-Wendroff code discussed previously with the streamwise pressure gradient term included. Cases of high shear and high pressure gradient, similar to that found on the leading edge of a wing ($c_f = 0.01$ and $dC_p/dx = -0.42$ /in.), and also cases of low shear and moderate pressure gradient ($c_f = 0.0005$ and $dC_p/dx = -0.05$/in.) were computed. For the worst case studied, the impact of pressure gradients was only 0.14% of c_f.

Shear Gradients and Resolution Issues

In applying the FISF method, one needs to know what physical location on the surface to ascribe the τ_w measurement to. In a zero stress gradient situation, the correct measurement location is at the leading edge of the oil. The reasoning for this is that under the condition of zero stress gradient (the assumption in the derivation of eq. 1), as shown previously, the streamwise oil thickness variation is linear. This fact combined with the fact that equation 3 is a hyperbolic equation (if $\partial \tau_w / \partial x = 0$) and has characteristic curves of $\frac{dx}{dt} = \frac{h\tau_w}{\mu_o} = const.$, which have positive slope for all physically realizable initial oil distributions, means that the slope of the oil, near the leading edge, is governed solely by the flow upstream of the oil's leading edge, hence the τ_w measured is the value at the leading edge location.

It is virtually impossible to image the oil leading edge directly, but by inference its position is located $\frac{1}{2}\Delta s_{2-1}$ upstream of s_1. This can be easily demonstrated by using the oil heights $h_1 = \lambda/4n_o$ and $h_2 = 3\lambda/4n_o$ at the first and second fringe peaks of destructive interference locations s_1 and s_2 and by the fact that the oil's profile is linear.

The spatial resolution of the FISF method is dependent on the fringe spacing, which, in turn, is dependent on the skin friction level, wavelength of the light source, oil viscosity, and wind tunnel run time. The highest spatial resolution is obtained by using only the first fringe. It turns out that the greatest accuracy is also achieved when only the first fringe is used provided the shear gradient level is low to moderate ($\Delta s_{3-2}/\Delta s_{2-1}$ of 0.9 to 1.1). For some cases where the shear gradient is high, greater accuracy can be achieved by using the first two fringes and the following relationship:

$$c_f = \frac{2n_o\mu_o}{q_\infty \lambda t}[\Delta s_{2-1} - 0.857(\Delta s_{3-2} - \Delta s_{2-1})] \tag{5}$$

This expression was arrived at through a minimization process wherein the constant (0.857, above) was varied until the difference between the c_f predicted from the above equation and the value prescribed at the leading edge of the oil in a numerical solution of equation 3 was a minimum over a range of shear and shear gradient levels ($-0.015 \leq dc_f/dx \geq 0.015$ /in., which are the maximum gradient levels typically encountered on wings and $0.002 \leq c_f \geq 0.01$). Note that equation 1 is recovered when $\Delta s_{3-2} = \Delta s_{2-1}$ (zero shear gradient).

A comparison of the predicted c_f values from equations 5 and 1 are shown in figure 6 for various different skin friction gradient levels. The comparison shows that equation 5 is clearly superior to that of equation 1 for this modeled situation. In practice, one has to trade off the reduction in fringe spacing accuracy, which generally results when two fringes are used, versus the increase in accuracy obtained by inclusion of shear gradient effects to determine whether equation 5 offers any advantage over equation 1. An uncertainty analysis, shown in a later section of this paper, show examples of situations where use of equation 5 is preferred.

Locating the leading edge of the oil patch, in a flow with a shear gradient, is slightly more complicated than in the gradient-free case. For cases with a shear gradient, the cross section of the oil is no longer linear but can be approximately described by a quadratic function $h = a_0 + a_1 s + a_2 s^2$. The unknown coefficients a can be determined by using the facts that $h = \lambda/4n_o$ at s of the first destructive interference location, $h = 3\lambda/4n_o$ at the second, and $h = 5\lambda/4n_o$ at the third. No simple closed form solution has been found (even though it is likely that one exists) but it is a straightforward task to find the coefficients and roots of this polynomial numerically.
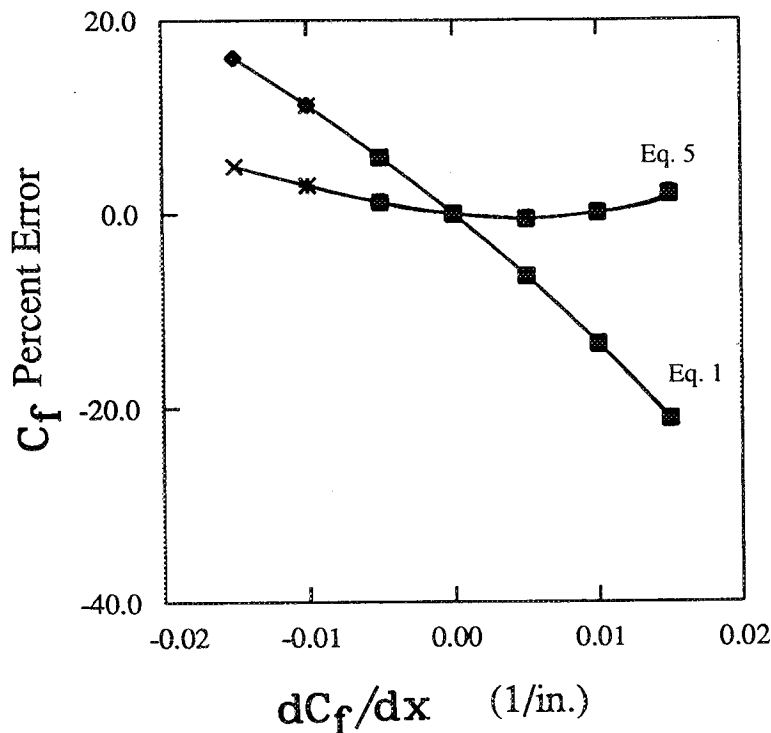

Figure 6. Comparison of equations 1 and 5 in a modeled shear gradient.

16

Often, it is desirable to be able to quote a numerical spatial resolution value for a measurement. In a three-dimensional flow, such a number for the FISF technique must have a component in the surface that is perpendicular to the skin friction direction (measurement volume width). Since one of the key assumptions in the derivation of equation 1 is that the oil flow is locally two-dimensional, it stands to reason that the measurement volume width must be at least 50 times the thickness of the oil for a locally two-dimensional approximation to be reasonably accurate. For a one-fringe space measurement, taking into account the way the fringe spacing algorithm functions, the measurement volume length would be approximately $\frac{7}{8}\Delta s_{2-1}$ and the width would be $50 \times (\frac{3\lambda}{2n_o})$ (if $\lambda = 2.13 \times 10^{-5}$ in. or 542 nm, $n_o = 1.4$, $\Delta s_{2-1} = 0.12$ in., then measurement volume length = 0.105 in. and width = 0.0012 in.) Note that for most CCD based imaging systems, the measurement volume width is sub pixel. Additional numerical experiments should be performed to confirm this spatial resolution analysis.

Extension to Three Dimensions

The FISF method developed in reference 2 is a two-dimensional technique that can readily be extended to three dimensions if a drop of oil is used as opposed to a line of oil. The skin friction magnitude is determined, as before, by measuring the fringe spacing. The direction of the skin friction vector is found by determining the orientation of the oil pathline measured in the vicinity of the leading edge of the oil relative to a fixed coordinate system. The essence of this idea was originally proposed in reference 5, and comparisons of τ_w from interferograms of oil lines and drops in a two-dimensional flow were made, but the potential of this approach was not further developed.

The main issue concerning the use of a drop is whether the assumptions used in deriving equation 1 are valid. This appears to be the case, as shown in figure 7 where a comparison of the fringe-spacing time histories of a line and drop are presented (note that in fig. 7 the Lax-Wendroff and linear solution results are for the oil-line case and are indistinguishable from each other). These data were measured in the two-dimensional channel facility. One can see that the measured fringe spacing is the same for a drop and a line within the accuracy limits of the FISF technique. This should not be a total surprise because the high initial oil thinning rate quickly drives even a very small drop to within the bounds of the underlying assumption of a two-dimensional flow (on the symmetry plane of the drop).

As will be shown later, in the case of two-dimensional flow, the total c_f measurement uncertainty is less for the oil-line case in comparison to oil drops, but in a three-dimensional flow the uncertainty is approximately the same. The use of oil drops has the added advantage of allowing one to determine the c_f vector direction.

To maximize the directional accuracy, the size of the drop should be made as small as the imaging system will allow. To maintain the assumption of a locally two-dimensional oil flow, the drop-diameter lower limit is quite small (roughly $50 \times \frac{3\lambda}{2n_o}$ or 0.0012 in.).

Shown in figure 8 is a comparison of fringe patterns for a drop and line taken in the channel flow facility on an Ultem 1000 surface. The fringes created by the drops are curved but the fringe spacing is relatively constant across the drop. At the extreme edges of the drop, the curvature of the fringe pattern is the greatest, giving a visual indication of where oil thickness variation violates the assumptions of the FISF technique.
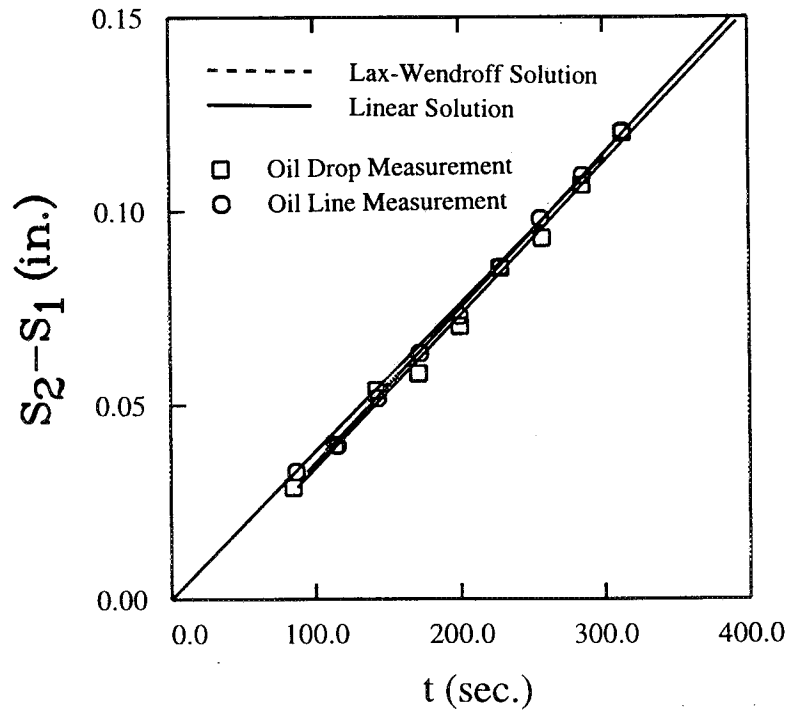
17

Figure 7. Comparison of measured and modeled drop and line fringe spacings, $\tau_w = 0.05$ psf $(c_f = 0.00485, q_\infty = 10.39$ psf) and $\nu_o = 50$ cs.
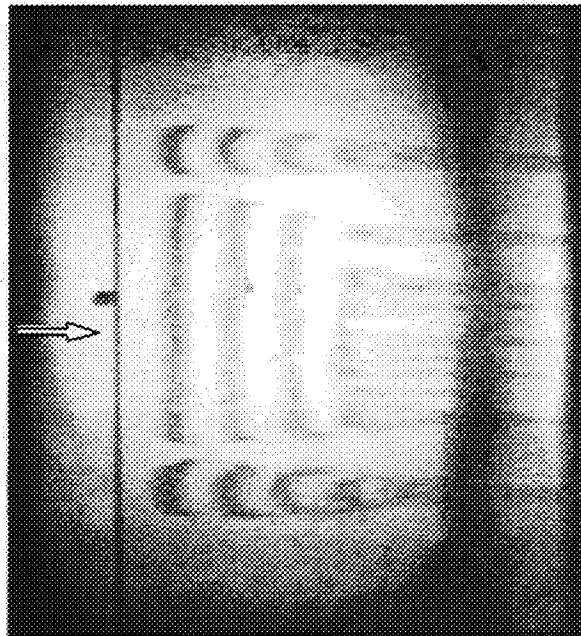

Figure 8. Oil flow originating from a line and also drops of oil placed on a black Ultem 1000 surface.

18

To demonstrate the capability of this approach to a greater degree, the skin friction distribution (magnitude and direction) along a spanwise oriented line on the surface of a wingtip (directly under the streamwise wingtip vortex) was measured and compared to Reynolds-averaged Navier-Stokes (RANS) predictions. The Reynolds number was 4.6 million, $\alpha = 10°$, and the boundary layer was tripped near the naturally ocurring transition location of 2% chord. In the RANS computations, the Baldwin-Barth (B-B) and the Spalart-Allmaras (S-A) turbulence models were used on grids of $115 \times 157 \times 83$ and $115 \times 189 \times 115$ points respectively. For further information on the computational approach and also for the complete computed wingtip-vortex surface c_f distribution, see reference 14.

Figure 9 shows a typical image of the wingtip oil-drop fringes, and the the c_f comparison is shown in figure 10. The agreement with these state-of-the-art computations is poor. In a sense, this is a welcome result because the discrepancy can mostly be attributed to the inability of turbulence models to function correctly in highly three-dimensional flows and underscores the need for accurate τ_w measurements in such flows.

In preparation for these measurements, a flat-bed pen plotter was used to draw and label a 12×16 fiducial grid (0.62 in. square cells) on 8 1/2 in. by 11 in. sheets of 2 mil black Ultem 1000. These sheets were then adhered to the suction side of the the wing surface using 3M General Purpose Spray Adhesive 201 (3M Adhesive Systems, St. Paul MN). The edges were further bonded using cyanoacrylate.

There is one small complication with the extension of the FISF approach to three dimensions, that being the effects of surface streamline convergence or divergence in the air and oil flows. The main difficulty is that equation 1 was derived based on the assumption of parallel limiting streamlines. In virtually all three-dimensional flows, streamline divergence is present to some degree but, fortunately,
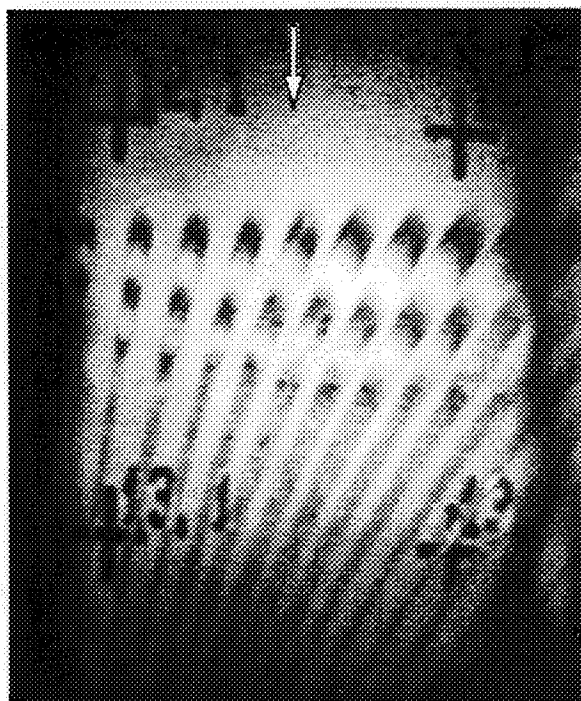

Figure 9. Oil flow originating from drops of oil on a black Ultem 1000 film under a wingtip vortex.
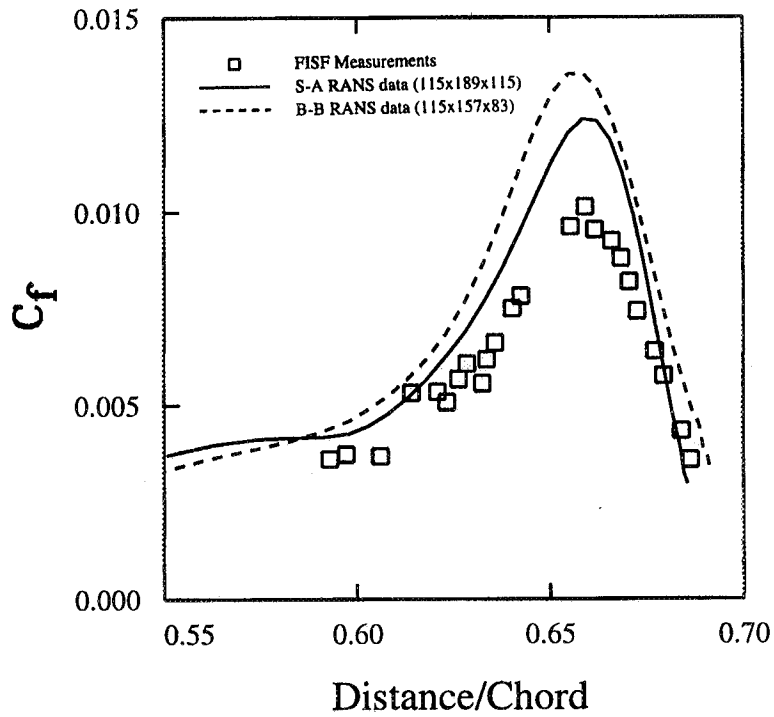
Figure 10(a). Measured skin friction magnitude on a surface under a wingtip vortex at $Re_c = 4.6 \times 10^6$ compared with RANS computational result (see ref. 14).
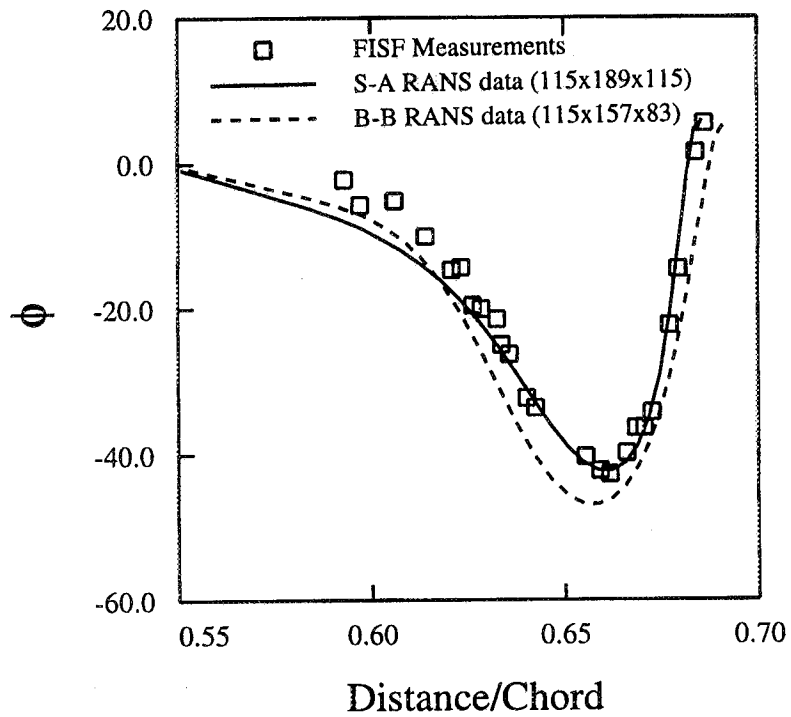

Figure 10(b). Measured skin friction direction on a surface under a wingtip vortex at $Re_c = 4.6 \times 10^6$ compared with RANS computational result (see ref. 14).

its effect on the accuracy of an FISF measurement is thought to be small except possibly in the vicinity of some types of critical points, shocks, and flow separations.

Building on the oil film control volume analysis presented in references 2 and 3 and referring to figure 1, it can be shown that if w_1 is the distance between two adjacent streamlines at the location of the first line of destructive interference and w_n is the distance at the nth fringe (where n is typically 1 or 2 depending on the number of fringes used in the measurement), then for small streamline convergence or divergence (w_n/w_1 between 0.8 and 1.2) $c_{f,actual} = \frac{1}{4}[5 - w_n/w_1]c_{f,measured}$.

If it is anticipated that streamline divergence is going to be large in a particular region of interest, μ_o and t can usually be chosen such that the effects of streamline divergence on the FISF accuracy is minimized (to a fraction of a percent) provided the imaging system has sufficient resolution.

Along these lines, the author has observed that oil streamline convergence occurs, to some degree, even in nominally two-dimensional flows. The channel flow results of figure 8, which were obtained under zero shear gradient conditions, show a degree of oil-flow convergence even though the air-flow streamlines are parallel. This can be seen by observing that the pathlines which the two drops trace out are straight, yet the side edges of oil drops converge. Similar behavior has been observed on a wing surface directly under a strong wingtip vortex, where one might expect to find fairly high streamline divergence or convergence. Close examination of traditional oil flow visualizations indicated that the limiting streamlines were such that, on the scale of an FISF measurement, w_2/w_1 should be small (see fig. 9). Yet, if a single drop of oil is placed on the surface, the included angle between the side edges of the resulting flow was found to be up to 7 degrees. This leads to $w_2/w_1 = 0.8$ and a measured c_f that is 5% less than the actual c_f. This phenomenon is currently being further explored through extension of the CFD-FISF modeling effort to three dimensions.

Accuracy

An uncertainty estimation of the FISF technique can be logically broken down into two parts: c_f magnitude uncertainty and c_f direction uncertainty. The c_f magnitude uncertainty question revolves around the applicability of equation 1 and how accurately each quantity on the right-hand side of this equation can be determined. The c_f direction uncertainty determination is slightly more complicated because it is tied to how accurately a surface flow of oil follows the limiting streamlines.

The uncertainty analysis can be further broken down by considering the imaging, regression, and lubrication theory issues independently. In this context, "imaging" refers to the mapping of points on the test surface to computer memory, "regression" refers to extracting the fringe spacing from the data stored in computer memory, and "lubrication theory" refers to how well c_f can be determined by measuring the slope of an oil flow front.

The accuracy of the nonlinear regression based fringe spacing determination was evaluated by studying a model of a "typical" fringe in the presence of random noise for different combinations of pixels/fringe and peak-to-peak first-fringe intensities. The results are presented in figure 11 for a case with a 10 intensity level peak-to-peak noise superimposed on the intensity variation of the model interferogram. This noise level is comparable to what is observed in practice on a glass surface, using
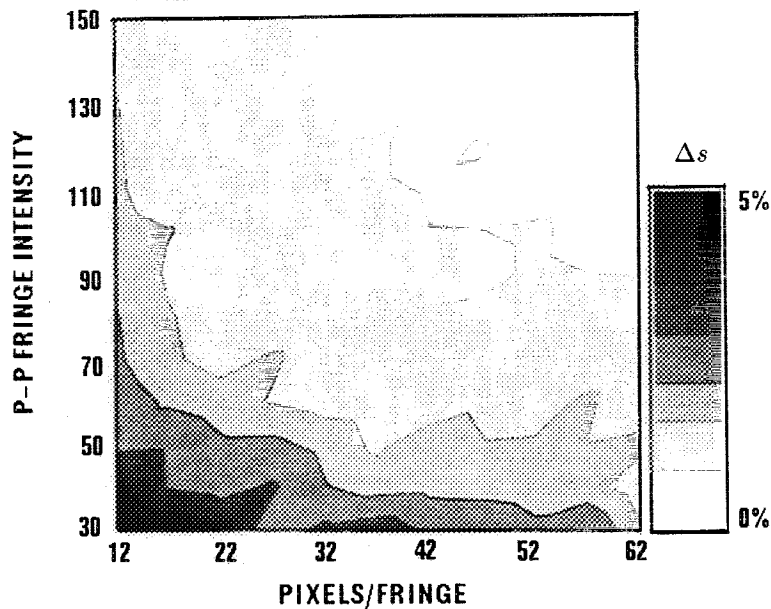
Figure 11. Nonlinear regression error (10 intensity level random noise case).

the Osram compact fluorescent light and an inexpensive 8-bit CCD camera as described previously. Each point on this figure is the average over 20 trials of the maximum fringe spacing error, found by the nonlinear regression for each trial, for a fixed random noise variation that was imposed on the model interferogram for 10 different phase relationships between the model and noise. In short, the regression was exercised 28,600 times in total for 2,860 different noise distributions to obtain the data in figure 11.

There are no surprises in the regression error trends shown in figure 11. The accuracy increases with increasing fringe visibility and also increasing fringe resolution. About the best regression accuracy that could be reasonably achieved in production wind tunnel tests is 2.1% assuming 30 pixels/fringe and an interferogram peak-to-peak intensity variation of 50. This is what is typically found on surfaces that have been coated with black high-gloss epoxy paint. On the other hand, if Ultem 1000 or Mylar sheets are used, 1% regression accuracy can be achieved with only 25 pixels/fringe. If a wind tunnel model constructed of high-refractive index glass ($n = 1.7$ to $n = 1.9$) was used, regression accuracies of better than 0.5% could be obtained.

The regression error analysis was partially validated by a test where the imaging/regression portions of the instrument were tested by imaging a card that had a sine-wave intensity variation printed on it (by a gray scale printer). The sine-wave image had about 50 pixels (per wavelength) and had a peak-to-peak intensity variation of 100 intensity levels. The RMS error of the identified fringe spacing was 1.15% for 15 trials.

Presented in table 2 is a listing of all of the significant FISF error sources identified in the current study. Associated with each error source is an uncertainty range which is considered to be representative of what can be expected depending on the quality of the instrumentation used and the flow situation being studied. The information in this table can be used to estimate the total uncertainty by applying the constant-odds uncertainty analysis technique of reference 15.

22

Table 2. FISF error sources

Error source	Uncertainty range	Remarks
Oil initial condition	-0.03% to -0.2% of c_f	Depends on μ_o and t (see fig. 3). Always a negative contribution to the total error.
Oil streamline curvature errors	0% to 5% of c_f	$c_{f,actual} = \frac{1}{4}[5 - w_n/w_1]c_{f,measured}$. Usually a positive error that can be minimized by using oil line (instead of drops).
Oil viscosity	$\pm 0.2\%$ to $\pm 5\%$ of ν_o	Low error achieved by calibrating oil using a viscometer. Manufacturer's ν_o specification is $\pm 5\%$.
Temperature	$\pm 0.05\%$ to $\pm 1\%$ of T_o	ν_o (and hence, c_f) changes 1% per $^\circ$F.
Light source wavelength	very small	Theoretically, fluorescent light spectrum is very stable (should be studied further).
Oil index of refraction	$\pm 0.015\%$ of n_o	An Abbe refractometer was used to measure n_o. Note that n_o is slightly temperature dependent.
Freestream dynamic pressure	$\pm 0.25\%$ to $\pm 1.0\%$ of q_∞	Dependent on pressure transducer quality.
dP/ds	$\pm 0\%$ to $\pm 0.14\%$ of c_f	See previously described numerical experiments.
$d\tau_w/ds$	$\pm 0\%$ to $\pm 20\%$ of c_f	Error level may be reduced by using equation 5 (see fig. 6).
Regression and imaging errors	$\pm 0.5\%$ to $\pm 5\%$ of Δs	Includes all CCD camera, frame grabber, and nonlinear regression errors except lens distortion errors (see fig. 11).
Lens distortion errors	$\pm 0\%$ to $\pm 1.4\%$ of Δs	Barrel or pincushion type distortions are most prevalent. $\Delta r = K_1 r^3$ describes pincushion distortion. Can be corrected for.
Startup and shutdown c_f errors	$\pm 0\%$ to ?	Can be the largest error source. Level is a function of wind tunnel startup and shutdown characteristics and c_f-Reynolds and Mach number dependency.

The total uncertainties for several FISF measurement system applications are listed in table 3.

The lens distortion uncertainty range listed in table 2 assumes that the principal lens distortion present is of pincushion (or barrel) type. Usually, this is the predominant type of distortion present when viewing a flat surface, with the axis of the camera normal to the surface, using the optical setup shown in figure 4. The distortion level of the 8 mm lens used in the current study was evaluated by imaging a grid (0.125 in.^{2} graph paper) and analyzing the discrepancy between the ideal and actual pixel locations of the grid-line intersections. It was found that the pincushion distortion could be described by $\Delta r = 0.018 r^3$ where Δr in inches is the difference between the ideal and actual radial distance r (in inches) measured from the center of the image as viewed by the lens to points near the frame

Table 3. Summary of FISF uncertainty

Case	$\%c_f$ uncertainty (eq. 1)	$\%c_f$ uncertainty (eq. 5)
FISF-channel flow results of fig. 7	4.9	8.9
Best possible FISF-channel flow result	2.8	3.8
FISF-wingtip (low quality)	9.3	13.6
FISF-wingtip results of fig. 10	6.1	6.2
Best possible FISF-wingtip result	5.8	4.5

boundaries (ref. 16). It is a relatively simple task to correct for this type of distortion, but the approach taken in the current study was to minimize the effects by restricting measurements to the center half of the lens viewing area. If one is viewing a curved surface or viewing off axis, other types of distortions will be present and should be accounted for.

In table 3, the uncertainty estimates presented assume no shear or pressure gradients for the channel flow cases and a shear gradient of 0.0006/in. in the wingtip cases. In all cases, uncertainties owing to oil initial conditions, light source wavelength variations, oil index of refraction variations, pressure gradients, and tunnel startup and shutdown effects have been neglected because they were considered to be too small to impact the total uncertainty of the c_f measurements. It has been assumed that an oil drop has been used and that the effects of streamline convergence, equivalent to $w_2/w_1 = 0.9$, have been included as an uncertainty source even though this effect could be accounted for through use of a correction.

The "best" estimates were obtained by assuming that the oil was calibrated with uncertainty of $\pm0.2\%$ of ν_o, and an oil temperature uncertainty of $\pm0.75°F$ for the wingtip case and $\pm0.25°F$ for the channel flow case. A fringe-spacing uncertainty of $\pm1.5\%$ of Δs (fringe spacing error is the sum of imaging, regression, and lens distortion uncertainties) has been included. The "low quality" wingtip case assumes use of uncalibrated oil with a $\pm5.0\%$ of ν_o uncertainty and a temperature uncertainty of $\pm1.5°F$.

As one can see, equation 5 does not offer a substantial advantage over equation 1 in most cases, but if a way can be found to decrease the uncertainty of the fringe spacing to less than $\pm1.5\%$ of Δs, the uncertainty associated with equation 5 will be less than that of equation 1 in high shear-gradient flows. For instance, a fringe spacing error of $\pm0.75\%$ of Δs leads to the total uncertainty of the "best possible wingtip result" of only 3.6% of c_f when using equation 5. The "FISF-wingtip results of figure 10" uncertainty estimate of table 3 is representative of what one might encounter in a typical subsonic wind tunnel test.

The c_f vector direction uncertainty is primarily dependent on the level of distortion present in the image caused by the optical components of the FISF system and surface registration errors arising from surface curvature and non-normal viewing angle effects. If errors of these types are not present, resolution of the imaging system is the limiting factor and it is relatively easy to demonstrate that the

vector direction can be determined to within ± 0.2 degree for an imaging system with 230 pixels/in. and a fringe spacing of 0.1 in. This uncertainty limit is nearly achieved when performing an FISF measurement on a flat surface with a normal viewing angle and using the center of the lens field of view as was done for the channel flow cases.

When performing measurements of greater complexity (e.g., wingtip case), it is often necessary to use as much of the lens field of view as possible. Pincushion distortion, if not corrected for, can cause relatively large c_f directional inaccuracies. For the 8 mm Computar model T0812FICS lens (Computar Inc., Japan) used in the current study, $\Delta\theta = 0.98r^3$ (θ in degrees and r in inches) describes the maximum angle error which approaches 2 degrees at the extreme edges of the lens field of view. If measurements are limited to the center half of the viewing area, the maximum angle error is about 0.5 degree. These numbers underscore the point that money spent on a good lens is not wasted.

A second c_f vector direction issue concerns the degree to which the oil flow deviates from the direction of the shear stress vector. Squire (ref. 9) performed an analysis which shows that the thinner the initial oil thickness (or drop maximum height) the closer the oil follows the actual surface skin friction direction. His analysis shows that the viscosity of the oil has no effect on the directional accuracy. This issue needs further study but it seems clear that if the characteristic length of the wind tunnel model being studied is large in comparison to the drop size, the oil pathline error is negligible in comparison to other directional errors.

Practical Aspects

There are several subtle points to the FISF technique that one learns from experience. If the test surface is a high-gloss painted surface, allow the paint to dry for at least 48 hours—but not too long, because eventually the gloss surface will dull. Virtually any cleaning (or polishing) agent will change the optical properties of a painted or plastic surface. Ideally, the best painted surface is an untouched one although, in practice, it is occasionally necessary to redo a case. The author has found that non-abrasive wipes such as those used in clean-room applications (Hydroentangled 100% polyester, Tech Spray Inc. Amarillo, TX 79105) work very well at removing oil without damaging the surface. It is important that as much of the oil be removed as possible if additional measurements are going to be made at the same spot. Another good practice is to start oil application at the downstream locations and work upstream in subsequent wind tunnel runs thereby reducing or possibly eliminating model cleaning.

The author has run into difficulties with dust, water vapor condensation, and lubricating oil from associated wind tunnel machinery. In one case, dust from the environment was entrained into a jet and deposited on the top of the silicone oil layer which, in the process, obliterated the fringes. In another case, FISF measurements on a cone in supersonic flow failed owing to condensation when the wind tunnel wall was removed. During the run, the model surface temperature decreased to nearly $0°F$. Upon opening the test section, the water vapor in the air immediately condensed on the surface of the cold model destroying any possibility of obtaining a measurement. Lubricating oil from compressors and moving machinery in the flow can also cause problems. In most cases, these types of problems can be worked around. For instance, a telescope mounted on a traverse stage was used to measure the fringe spacing through the glass of the test section wall in the case of the supersonic cone experiment.

Wind tunnel startup and shutdown (off condition) time can be quite long in some large facilities. As pointed out in reference 2, this effect can be partially accounted for by replacing the product $q_\infty t$ in equations 5 or 1 with $\int_0^{t_{run}} q_\infty dt$ and using an average surface temperature when obtaining the oil properties. This modification has no effect on the physical fact that the Reynolds number and consequently, in most cases, the skin friction varies when off condition, but it does normalize the τ_w data so that consistent results may be obtained from wind tunnel run to run. It should be noted that for cases where c_f is not dependent on Reynolds or Mach number (i.e., incompressible tripped flows), wind tunnel transient effects do not impact on FISF measurements provided the integral approach is used. Alternatively, the effects of the startup and shutdown can be avoided by measuring the time variation of the fringe pattern as in reference 17 provided the measurement locations can be viewed during a run. Note that the other extreme (a too rapid startup of a tunnel) should also be avoided in order to prevent waves on the surface of the oil. These waves were studied in reference 8 but their origin remains unknown.

Application of an array of oil drops was accomplished by dipping a hard plastic hair comb into a plastic tray containing the oil and then touching the comb to the surface being studied. For surfaces with curvature, this technique does not work well and an alternative approach of placing individual drops using a glass rod with a round tip was used. The size of the drops can be roughly controlled by varying the size of the applicator and the depth of the oil in the tray.

The silicone oil used in the current study, and in the majority of the referenced reports, is Dow Corning 200 Fluid (Midland, MI). This fluid is a polydimethyl-siloxane polymer and is available with the physical properties listed in table 4.

Table 4. Physical properties of Dow Corning 200 fluid (ref. 18, properties at 77°F or 25°C)

$\nu_{o,nom}$	cs	10	50	100	200	350	500	1000	10,000	12,500	30,000
γ_o	–	0.934	0.960	0.964	0.967	0.968	0.969	0.970	–	–	0.971
n_o	–	–	1.4022	1.4030	1.4032	1.4034	1.4034	1.4035	1.4036	1.4036	1.4037
α_o	$\frac{cc}{cc}/°C$	0.00108	0.00104	0.00096	0.00096	0.00096	0.00096	0.00096	–	0.00096	0.00096

The manufacturer's specifications for the kinematic viscosity is $\pm 5\%$ which, if truly representative of the bottle-to-bottle viscosity variation, implies that the oil should be calibrated prior to FISF use. The viscosity, as measured by Dow Corning at the time of manufature and reported on certificates of analysis (available on request from Dow Corning), was checked for several different lot numbers. The worst case was 4.11% difference between the nominal viscosity printed on the bottle label and that reported on the certificate of analysis.

Several commonly used viscosity measurement techniques are suitable for the purpose of oil calibration. A calibrated kinematic viscometer tube with accuracy of $\pm 0.2\%$ is available from Fisher Scientific (Pittsburgh, PA) and is relatively simple to use, but virtually all the available techniques require accurate knowledge of the oil temperature (usually, viscosity measurements are performed in a temperature controlled water bath).

Since it is not practical to calibrate oil over a range of temperature, other means are required to determine the oil viscosity variation with temperature. Equation 6 serves this purpose. The basic form of equation 6 is similar to that found in many textbooks for the viscosity-temperature dependence of liquids.

The best oil-viscosity calibration approach is to calibrate the oil at the temperature at which it will be used or as close to it as possible. Use of equation 6 allows one to accurately determine oil viscosity at temperatures other than that of the oil-viscosity calibration. For example, if the viscosity of the oil $\nu_{o,cal}$ is measured at temperature T_{cal}, then the viscosity $\nu_{o,T}$ at T of a wind tunnel test can be determined with a typical accuracy of 0.12% of ν per °F of the temperature difference $T - T_{cal}$ (in addition to the $\nu_{o,cal}$ uncertainty).

$$\nu_{o,T} = Exp\left[\frac{C_1}{T + C_2} - \frac{C_1}{T_{cal} + C_2} + LOG_{10}(\nu_{o,cal})\right] \tag{6}$$

where T is in degrees Kelvin, $C_1 = 774.8622$, and $C_2 = 2.6486$. This equation is most accurate for $255 \leq T \geq 310$ K ($0 \leq T \geq 100$°F) and for $100 \leq \nu_{o,cal} \geq 1000$.

Furthermore, the density of the oil is also slightly dependent on temperature. The manufacturer provides the following relationship for the oil's specific gravity at a temperature T:

$$\gamma_{o,T} = \frac{\gamma_{o,T=25°C}}{1 + \alpha[T - 25]} \tag{7}$$

where the coefficient of expansion α is given in table 4 and T is in °C. Hence $\rho_{o,T} = (\gamma_{o,T})\rho_{H_2O,T=25°C}$ and determination of μ_o is a trivial task.

The question of what is the optimal length of time to expose the oil to the flow is difficult to answer. If t is too short, the resolution of the imaging system will not be sufficient to accurately image the fringes. On the other hand, experience has shown that the fringe visibility decreases if the run time is excessive (probably caused by contamination of the oil by particulate and water vapor). In the current study, good results were usually obtained when the viscosity of the oil was chosen such that $150 \leq t \leq 300$ sec and number of pixels per fringe was 30 to 40 (0.10 to 0.15 in. fringe spacing).

To avoid degradation of the fringes by dust and/or humidity, it is important to image the fringes as soon as possible after turning off the flow. A trigger button mounted on the side of the FISF instrument box made it possible to image 15 frames (each at a different location on the model) in a period of a few minutes.

There appears to be a correlation between humidity and fringe life. This correlation is not supported by the results of others who have obtained good FISF measurements during flight tests under high relative humidity conditions. In the current study, 50% relative humidity was found to be the approximate upper limit for good FISF results. It is not clear why fringe visibility would be affected by humidity. A

possibility is that water vapor in the air, under high humidity conditions, gets deposited on the surface of the oil causing speckle and therefore, reduced fringe visibility.

CONCLUSIONS

In an effort to obtain an accurate, reliable, and easy to use skin friction measurement technique for three-dimensional flows, several enhancements have been made to the fringe-imaging skin friction technique of reference 2. Most important is the extension of the FISF technique to three dimensions, which was achieved by using drops of oil (as opposed to the line of oil used in the original approach). Additional noteworthy improvements include a new skin friction data reduction formula for flows with shear gradients, development of a nonlinear regression approach to fringe analysis, and the development of a PC-based application for FISF measurements. The hardware developed is relatively inexpensive and the software has been made available.

Extensive use of modeling and benchtop tests have verified the new FISF approach. The overall accuracy range was found to be $\pm 2.8\%$ to $\pm 13.6\%$ of c_f and ± 1 degree directional accuracy depending on the instrumentation used and flow being studied. A comparison of c_f measured on a wingtip with computed Reynolds-averaged Navier-Stokes results showed large differences. This disagreement, which is thought to be a turbulence modeling deficiency, serves to reaffirm the importance of skin friction measurements.

28

APPENDIX

A personal computer application (cxwin1g) has been written that automates several aspects of the FISF technique, including image acquisition, nonlinear regression fringe analysis and skin friction computation. Use of this application in conjunction with a frame grabber and the FISF-CCD based imaging system (or equivalent) will allow one to rapidly obtain accurate skin friction data.

The source code, an executable, and some utility programs are currently in the process of being released by COSMIC. This application was developed on a 486-33 machine running Windows 3.1 and has been tested on several other machines. The minimum RAM memory requirement is 8 megabytes. Either a VGA, super VGA, or EGA video card is required. The application has a built-in capability to grab and display images provided that the ImageNation (Beaverton, OR) CX100 board has been installed. For systems where this board is not present, the Fileit utility can be used to convert several commonly used image file formats to the ".bin" format which cxwin1g reads or one can modify the source code to work with other frame grabbers. To use Fileit, type "Fileit infile.tif outfile.bin" at the command line prompt. Fileit converts gif, tif, tga, tif, wpg, pic, and pcx files.

The Microsoft Windows application is a mixed language application that was developed using Microsoft Visual C++ version 1.00 and Microsoft Fortran version 5.1. The main program and most of the image processing related routines are coded in ANSI C, and the nonlinear regression related routines are coded in Fortran and called by the C main program. In the event that recompilation of any of the cxwin1g C modules becomes necessary, it may be possible to link the recompiled C modules with the Fortran object modules provided on the disk, hence no Fortran compiler would be required. The .mak file included on the floppy disk shows the necessary C compiler options required to recompile and link the application.

To install the application, simply create the directories c:\expskin and c:\expskin\data and copy the .exe file to c:\expskin and the default.dat and default.bas files to c:\expskin\data. A double click on the cxwin1g icon should start the application and the screen shown in figure 12 should appear (except with no fringe pattern visible).

If one is going to analyze an existing FISF fringe image, the corresponding binary image file should be placed in the c:\expskin\data subdirectory and it should have a file name of XXXXXXX.bin (where XXXXXXX are seven user defined characters that can be used to designate a run number or some other distinguishing characteristic subsequently referred to as the "Append characters"). The sequence of steps to obtain a skin friction result is as follows:

1. Click on the "Read File" button and the "Data" window will appear as shown in figure 13. Enter the appropriate quantities as required. Three freestream property data input options are available. One can enter q_∞ and T; or P_{total}, M_∞ and T; or $\int_0^{t_{run}} q_\infty dt$ and T. The choice is made by clicking on the desired radiobutton in the "Freestream Properties" section of the "Data" window. Only data for the user's choice need be entered. Units are cs for ν, nM for the light source wavelength, sec for t, in. H_2O for q_∞, °F for T, psi for P_{total}, and in. H_2O sec for $\int_0^{t_{run}} q_\infty dt$. The oil viscosity termed "Nom Kin Visc" is the oil kinematic viscosity at 77°F (25°C) in centistokes. If this value is not known, then equation 6 should be used to determine ν_o at 77°F.
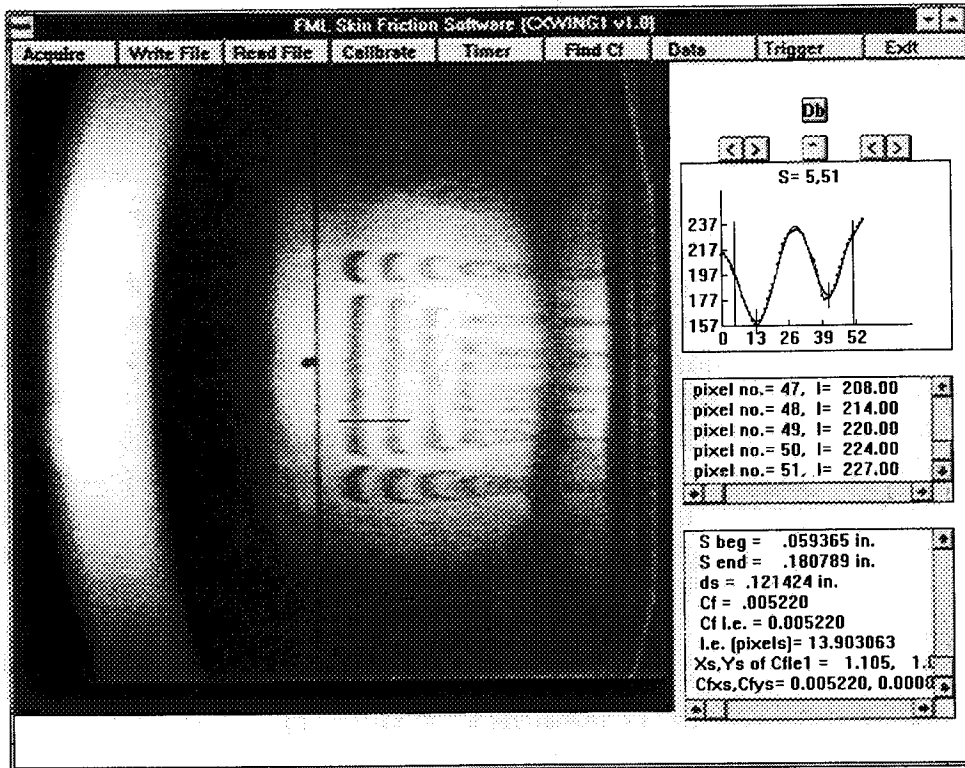
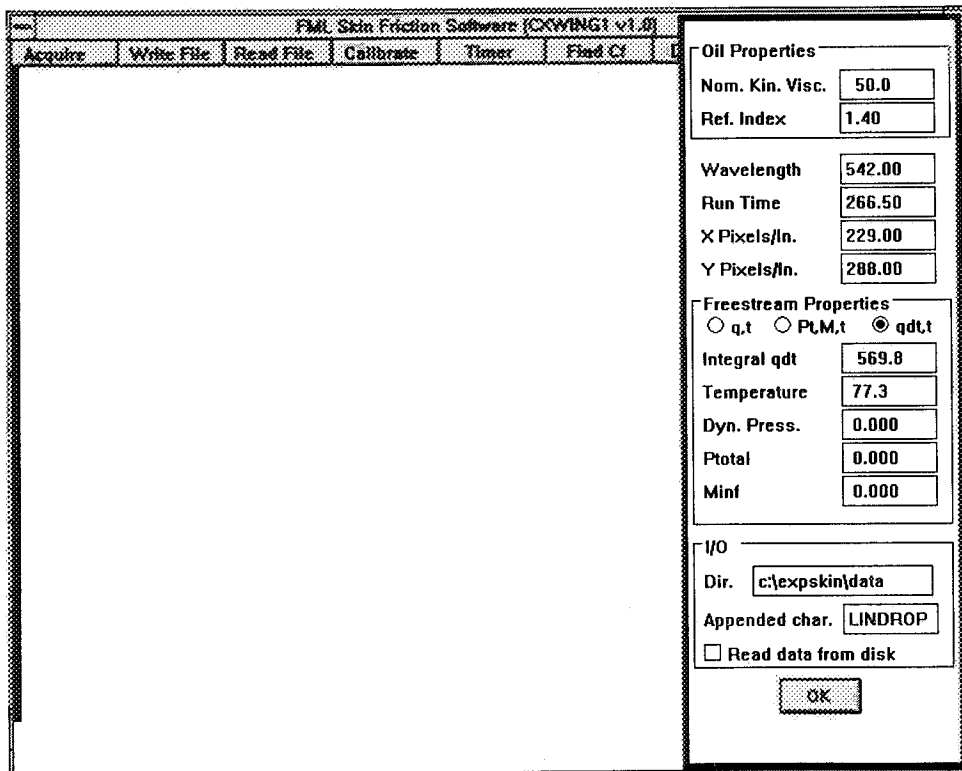Figure 12. Main window of skin friction application.

Figure 13. Data entry dialog box of skin friction application.

30

If a spatial calibration is going to be performed and the type of the calibration is type 1, no "X Pixels/In." or "Y Pixels/In." entry is required as these values will be determined during the calibration process. Alternately, if a type 2 calibration is to be performed, "X Pixels/In." and "Y Pixels/In." must be entered. These values are in terms of window coordinates where X is measured across top of screen and Y is down. Upon hitting the "Ok" button, cxwin1g will create a log file (filename XXXXXXX.log) in the c:\expskin\ data directory and a popup dialog box will appear that allows you to select and open the XXXXXXX.bin file. The desired image should appear in the main portion of the screen.

2. A spatial calibration can be performed using the "Calibrate " feature. In order to achieve a proper spatial calibration of the imaging system, an x-y reference axes system target must appear in the image's field of view. A draftsman's target or some other marking that denotes a known x-y position on the surface, the $+x$ and $+y$ axes directions, and, for calibration type 1, Δx and Δy may be used The simplest possible marking consists of three dots, the first located at a known surface location and the other two located at $+\Delta x, 0$ and $0, \Delta y$ respectively. All spatial dimension related quantities have units of inches.

Obviously, if the surface being imaged is highly curved, there is no way to obtain a proper registration of the surface using a one-camera system. Under this condition, an alternative method should be used to determine the measurement location on the surface and the magnification of the imaging system. The spatial calibration function does not have to be invoked. One can enter the number of pixels/inch in screen coordinates directly in the "Data" window if that information is already known although, without a spatial calibration, the reference system used to compute the skin-friction direction is based on the "screen coordinates" (which depend on the orientation of the CCD camera relative to the model).

To invoke the calibration, click on the "Calibrate" button. The calibration window will pop up as shown in figure 14. One of two calibration processes may be chosen. Calibration type 1 should be chosen if the magnification (pixels/inch in screen coordinates) of the imaging system is not known. Calibration type 2 is simpler and is most useful when processing a number of images where the distance from the lens to the model surface remains constant.

If calibration type 1 is chosen, enter the x, y position of the reference location and $+\Delta x, +\Delta y$ in the calibration dialog box. Next, position the crosshair over the reference position and click. Fine positioning of the crosshair can be accomplished using the arrows after the left mouse button has been depressed. Move the crosshair to the $+\Delta x$ position and click twice. Return the crosshair to the reference position and click. Finally, position the crosshair at the $+\Delta y$ location and click twice. Cxwin1g uses the information entered in the calibration dialog box along with the information entered via the mouse to determine the pixels/inch in the x and y directions and also the orientation of the surface coordinate system relative to the current camera or screen based coordinate system.

If calibration type 2 is chosen, enter the x, y position of the reference location in the calibration dialog box ("X Pixels/In." and "Y Pixels/In." should have been previously entered) and click on "Ok." Next, position the crosshair over the reference position and click. Move the crosshair to some point on the $+x$ axis and click twice. Return the crosshair to the reference position and click. Finally, position the crosshair at some point on the $+y$ axis and click twice.
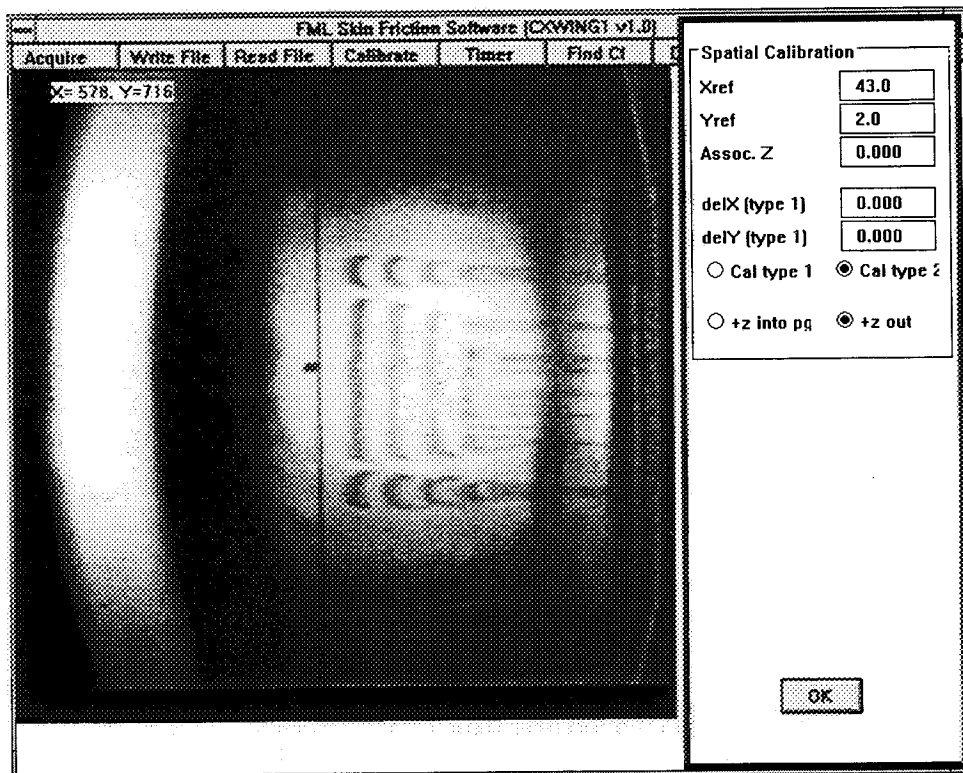
Figure 14. Spatial calibration dialog box of skin friction application.

Cxwin1g uses the information entered in the calibration dialog box along with the information entered via the mouse to determine the pixels/inch in the x and y directions and also the orientation of the surface coordinate (or model based) system relative to the current camera or screen based coordinate system. It should be noted that, provided that correct values for "X Pixels/In." and "Y Pixels/In." have been entered in the "Data" window, a spatial calibration is optional.

3. After step 2 has been completed, the application is fully calibrated. To obtain a skin friction result, position the crosshair upstream of the first band of destructive interference and click. Next, position the crosshair downstream of either the second or third band of destructive interference and click twice. The line drawn should be parallel to the direction of the surface shear vector as indicated by the direction of the oil flow.

The intensity data along the line joining these two points will appear in the line plot window in the upper right hand child window. To see an enlarged version of this plot, click on the "Λ" located above this window. To return the plot window to its initial size, click on the "Λ" again.

Two types of controls are provided to "window" the fringe intensity data. Gross control is achieved by clicking the right and left mouse buttons in the plot window to position the data limiting bars (right mouse button for the right bar and left mouse button for the left bar). Fine positioning can be done using the left-right arrows located above the plot. Use the plot window controls to position the data limiting bars so that they are approximately midway between the interference peaks upstream of the first

destructive interference band and downstream of the second or third destructive interference band. This windowing process will be indicated on the image and in the plot window by a color change to green. The purpose of windowing is to obtain the greatest accuracy by restricting the regression analysis to the first one or two fringes.

4. Click on "Get Cf" and, after a few seconds, a blue line (the nonlinear regression results) will appear in the line-plot child window and the c_f result will appear in the lower right-hand text window.

5. The results of the skin friction measurement can be saved in the ASCII database file c:\expskin \data\default.bas by hitting the "Db" button.

REFERENCES

1. Winter, K. G.: An Outline of the Techniques Available for the Measurement of Skin Friction in Turbulent Boundary Layers. Prog. Aerospace Sci., vol. 18, no. 1, 1977, pp. 1–57.

2. Monson, D. J.; and Mateer, G. G.: Boundary-Layer Transition and Global Skin Friction Measurements with an Oil-Fringe Imaging Technique. SAE 932550, Aerotech '93, Costa Mesa, CA, Sept. 27–30, 1993.

3. Tanner, L. H.; and Blows, L. G.: A Study of the Motion of Oil Films on Surfaces in Air Flow, with Application to the Measurement of Skin Friction. J. Physics E, vol. 9, 1976, pp. 194–202.

4. Tanner, L. H.: A Skin Friction Meter, Using the Viscosity Balance Principle, Suitable for Use with Flat or Curved Metal Surfaces. J. Physics E, vol. 10, 1977, pp. 278–284.

5. Tanner, L. H.; and Kulkarni, V. G.: The Viscosity Balance Method of Skin Friction Measurement: Further Developments Including Applications to Three-Dimensional Flow. J. Physics E, vol. 9, 1976, pp. 1114–1121.

6. Monson, D. J.; and Higuchi, H.: Skin Friction Measurements by a New Nonintrusive Double Laser Beam-Oil Viscosity Balance Technique. AIAA J., vol. 19, no. 6, 1980, pp. 739–744.

7. Westphal, R. V.; Bachalo, W. D.; and Houser, M. H.: Improved Skin Friction Interferometer. NASA TM-88216, 1986.

8. Murphy, J. D.; and Westphal, R. V.: The Laser-Interferometer Skin-Friction Meter: A Numerical and Experimental Study. J. Physics E, vol. 19, 1986, pp. 744–751.

9. Squire, L. C.: The Motion of a Thin Oil Sheet under the Steady, Boundary Layer on a Body. JFM, vol. 11, 1961, pp. 161–179.

10. Haver, R. J.: The Verdict is In: Solid-State Fluorescent Ballasts are Here. Electronic Design News, Nov. 5, 1976, pp. 65–69.

11. Chen, W. Y.; and Stegen, G. R.: Experiments with Maximum Entropy Power Spectra of Sinusoids. J. Geophys. Res., vol. 79, no. 20, 1974, pp. 3019–3022.

12. Schemm, J. B.; and Vest, C. M.: Fringe Pattern Recognition and Interpolation Using Nonlinear Regression Analysis. Applied Optics, vol. 22, no. 18, 1983, pp. 2850–2853.

13. Saunders, D. A.; Kennelly, R. A.; and Kennelly, L. C.: "Aerodynamics Division Software Library. NASA RP-1276, June 1992.

14. Dacles-Mariani, J.; Zilliac, G. G.; and Bradshaw, P.: Numerical/Experimental Study of a Wingtip Vortex in the Near Field. AIAA J., vol. 33, no. 9, 1995, pp. 1561–1568.

15. Kline, S. J.; and McClintock, F. A.: Describing Uncertainties in Single-Sample Experiments. Mech. Eng., Jan. 1953, p. 3.

16. Born, M.; and Wolf, E.: Principle of Optics. 3rd ed., Pergamon Press, Oxford, U.K., 1965.

17. Naughton, J. W.; and Brown, J. L.: Surface Interferometric Skin-Friction Technique. AIAA Paper 96-2183, New Orleans, LA, June 17–20, 1996.

18. Information About Dow Corning Silicone Fluids. Dow Corning Corp., Midland, MI, 1994.

REPORT DOCUMENTATION PAGE

Public reporting burden for this collection of information is estimated to average 1 hour per response, including the time for reviewing instructions, searching existing data sources, gathering and maintaining the data needed, and completing and reviewing the collection of information. Send comments regarding this burden estimate or any other aspect of this collection of information, including suggestions for reducing this burden, to Washington Headquarters Services, Directorate for information Operations and Reports, 1215 Jefferson Davis Highway, Suite 1204, Arlington, VA 22202-4302, and to the Office of Management and Budget, Paperwork Reduction Project (0704-0188), Washington, DC 20503.

1. AGENCY USE ONLY (Leave blank)	2. REPORT DATE December 1996	3. REPORT TYPE AND DATES COVERED Technical Memorandum

4. TITLE AND SUBTITLE

Further Developments of the Fringe-Imaging Skin Friction Technique

5. FUNDING NUMBERS

505-59-54

6. AUTHOR(S)

Gregory G. Zilliac

7. PERFORMING ORGANIZATION NAME(S) AND ADDRESS(ES)

Ames Research Center
Moffett Field, CA 94035-1000

8. PERFORMING ORGANIZATION REPORT NUMBER

A-965314

9. SPONSORING/MONITORING AGENCY NAME(S) AND ADDRESS(ES)

National Aeronautics and Space Administration
Washington, DC 20546-0001

10. SPONSORING/MONITORING AGENCY REPORT NUMBER

NASA TM-110425

11. SUPPLEMENTARY NOTES

Point of Contact: Gregory G. Zilliac, Ames Research Center, MS 260-1, Moffett Field, CA 94035-1000
(415) 604-3904

12a. DISTRIBUTION/AVAILABILITY STATEMENT

Unclassified — Unlimited
Subject Category 35

12b. DISTRIBUTION CODE

13. ABSTRACT (Maximum 200 words)

Various aspects and extensions of the Fringe-Imaging Skin Friction technique (FISF) have been explored through the use of several benchtop experiments and modeling. The technique has been extended to handle three-dimensional flow fields with mild shear gradients. The optical and imaging system has been refined and a PC-based application has been written that has made it possible to obtain high resolution skin friction field measurements in a resonable period of time. The improved method was tested on a wingtip and compared with Navier-Stokes computations. Additionally, a general approach to interferogram-fringe spacing analysis has been developed that should have applications in other areas of interferometry. A detailed error analysis of the FISF technique is also included.

14. SUBJECT TERMS

Skin friction, Fringe analysis, Imaging system

15. NUMBER OF PAGES
38

16. PRICE CODE
A03

17. SECURITY CLASSIFICATION OF REPORT Unclassified	18. SECURITY CLASSIFICATION OF THIS PAGE Unclassified	19. SECURITY CLASSIFICATION OF ABSTRACT	20. LIMITATION OF ABSTRACT

NSN 7540-01-280-5500